frontiers in Earth Science

ORIGINAL RESEARCH
published: 18 January 2022
doi: 10.3389/feart.2021.798701

The Karavansalija Mineralized Center at the Rogozna Mountains in SW Serbia: Magma Evolution and Time Relationship of Intrusive Events and Skarn Au ± Cu–Pb–Zn Mineralization

J. Hoerler[1], A. Von Quadt[1], R. Burkhard[1], I. Peytcheva[1,2], V. Cvetkovic[3] and T. Baker[4]*

[1]Institute of Geochemistry and Petrology, ETH Zurich, Zurich, Switzerland, [2]Geological Institute, Bulgarian Academy of Science, Sofia, Bulgaria, [3]Faculty of Mining and Geology, University of Belgrade, Belgrade, Serbia, [4]Eldorado Gold Corporation, Vancouver, BC, Canada

The Karavansalija Mineralized Center (KMC) with its Au–Cu skarn mineralization associated with the Rogozna Mountains magmatic suite in southwestern Serbia belongs to the Oligocene Serbo-Macedonian magmatic and metallogenic belt (SMM-MB). Samples from intrusive and volcanic rocks at the KMC show typical arc signatures of subduction-derived magmas through enrichment in large-ion lithophile elements (LILE) and depletion of high–field strength elements (HFSE). The magmas developed a high-K (calc-alkaline) fractionation trend and evolved toward shoshonitic compositions. Whole-rock trace element data suggest plagioclase-absent, high-pressure amphibole ± garnet fractionation that generates adakite-like hydrous magmas during evolution in lower crustal magma chambers. Zircon LA–ICP–MS and high-precision CA–ID–TIMS dating together with zircon trace elements and Hf isotope measurements were carried out in order to couple the geochronologic and geochemical evolution of the KMC. The results suggest that magmatism starts around 29.34 Ma with granitic to rhyodacitic subvolcanic intrusions followed by a more evolved magmatic intrusion that was emplaced into Cretaceous limestone, generating a widespread skarn alteration at ca. 28.96 Ma. After a period of quiescence of about 1.2 My, either another magma body evolved or the same upper crustal magma chamber was recharged and also likely partly reactivated older plutonic rocks as indicated by xenocrysts. The REE ratios shift from apatite, titanite ± amphibole-dominated fractionation of the older magmatic event to crystallization of allanite, efficiently depleting the LREE and Th/U in the younger upper crustal magma. After a lamproite-like melt was injected, the increased heat and fluid pressure led to the expulsion of a quartz-monzonite porphyritic stock at ca. 27.72 Ma, strongly interacting with the skarns and established a fertile hydrothermal system. Soon after a non-mineralized second pulse of some porphyry dykes cut the previous phenocryst-rich “crowded” porphyries and skarns at ca. 27.60 Ma, thus bracketing the maximum timespan of ore mineralization to about 112 ± 45 Ka. Increased contribution of a lamproite-like melt is inferred from the presence of phlogopite micro-phenocrysts, phlogopitization of biotite, and diopside clusters in the latest porphyry dykes. There is a trend of increased crustal

OPEN ACCESS

Edited by:
Bertrand Rottier,
Laval University, Canada

Reviewed by:
Kit Lai,
Universiti Brunei Darussalam, Brunei
Qihai Shu,
China University of Geosciences, China

***Correspondence:**
A. Von Quadt
vonquadt@erdw.ethz.ch

Specialty section:
This article was submitted to Economic Geology, a section of the journal Frontiers in Earth Science

Received: *20 October 2021*
Accepted: *29 November 2021*
Published: *18 January 2022*

Citation:
Hoerler J, Von Quadt A, Burkhard R, Peytcheva I, Cvetkovic V and Baker T (2022) The Karavansalija Mineralized Center at the Rogozna Mountains in SW Serbia: Magma Evolution and Time Relationship of Intrusive Events and Skarn Au ± Cu–Pb–Zn Mineralization. Front. Earth Sci. 9:798701. doi: 10.3389/feart.2021.798701

assimilation from the oldest volcanic phase to the emplacement of the youngest porphyry dykes recorded by ε-Hf of the zircons. Oligocene occurrences of significant base metal mineralization within Serbia, northern Macedonia, and Greece, e.g., Crnac, Rudnik, Veliki Majdan, Stratoniu, or the Cu–Au porphyry at Buchim (northern Macedonia), are all associated with trachy-andesitic (quartz latitic) porphyry dykes, which originated through post-collisional tectonic settings or upper plate extension involving reworking of crustal arc-derived rocks and partial melting of the mantle wedge. This study demonstrates that on the basis of field relationships and the application of high-precision CA-ID-TIMS zircon age data, pulses of porphyry dykes of a 10ka age range can be distinguished, and the timing of mineralization can be parenthized.

Keywords: ore deposits, exo/endoskarn, CA-U/Pb TIMS dating, Balkan Peninsula, magmatism, short life-time magmatic event

INTRODUCTION

Zircon geochemistry and geochronology are widely applied to improve our understanding of crustal magmatic systems and constrain timescales of geological processes, such as those forming events of economically important magmatic–hydrothermal Cu–Au–Mo deposits.

Metal deposits (Pb, Zn, Cu, and Au, among others) provide successive samples of magma extracted from crustal-scale hydrous magmatic systems, skarn reaction between granitic magmas and marbles including fluid-enriched solutions, or/and remobilization of the base metals out of the skarn into new-growing granodioritic dikes. They are, therefore, a critical source of information about the processes and rates of magma ascent, magma storage, and fluid generation, bridging those of volcanism and pluton formation. The identification of the processes that lead to skarn deposit formation (Meinert et al., 2005) and later to enrichment of "porphyry-like" intrusion dikes and the timescales on which they operate can provide us with valuable information about magmatic processes but could also potentially help in discriminating fertile magmatic systems from ubiquitous infertile systems, resulting in barren intrusions or volcanic eruptions.

Recent advances in high-precision zircon geochronology by chemical abrasion–isotope dilution–thermal ionization mass spectrometry (CA–ID–TIMS (Mattinson, 2005; Bowring et al., 2011; McLean et al., 2011; Condon et al., 2015; McLean et al., 2015) now allow dating of multiple intrusions associated with ore formation with unprecedented precision. The improved precision permits the constraint of rapid events, such as individual skarn and hydrothermal mineralization phases (<100 kyr; von Quadt et al., 2011; Buret et al., 2016; Tapster et al., 2016), that typically occur during a long term period of volcanism and intrusive magma emplacement extending over several million years (Halter et al., 2004; Rohrlach and Loucks, 2005; Maksaev et al., 2006; Lee et al., 2017). The integration of the chemical information gained from zircon can yield time-calibrated information about magma chemistry, thermal evolution, and mixing processes during zircon crystallization in magmatic systems (Chelle-Michou et al., 2014; Samperton et al., 2015; Buret et al., 2016; Szymanowski et al., 2017).

Geological timescales for magmatic and hydrothermal processes involved in ore formation have been suggested based on *in situ* LA–ICP–MS U–Pb data (Banik et al., 2017; Lee et al., 2017; Garwin, 2000) and CA–ID–TIMS geochronology, which became increasingly precise (von Quadt et al., 2011; Lehmann et al., 2013; Chelle-Michou et al., 2014; Tapster et al., 2016; Large et al., 2018). However, several studies applying multiple techniques to the same sample sets have resulted in variable dates (von Quadt et al., 2011; Chiaradia et al., 2013; Chiaradia et al., 2014; Chelle-Michou et al., 2014). The discrepancy demands a more detailed understanding of the precision and accuracy of the techniques and statistical data treatment that are applied to derive a geological age.

For the present study, we obtained a large dataset of zircon geochemistry and geochronology by laser ablation inductively coupled plasma mass spectrometry (LA–ICP–MS) followed by high-precision geochronology of the same zircon crystals, utilizing the CA–ID–TIMS technique. This study focuses on a regional suite of predominantly calc-alkaline granitoid rocks, which crop out along the border between the easternmost Vardar zone and Serbo-Macedonian Massif (**Figure 1**). We focus on the Karavansalija Mineralized Center (KMC) that lies within the base metal–dominated area of the Serbo-Macedonian magmatic and metallogenic belt (SMMMB) surrounded by the Cenozoic magmatic intrusives and extrusives of the Rogozna mountains (Serbia; **Figures 1–3**). The KMC was mentioned as an occurrence of Au–Cu mineralization with secondary base-metal enrichments, which is distal to known deposits in the Rogozna Mountains (Urosević, M. et al., 1973; Kandić, M. et al., 1987). The ore mineralization is described by Budinov et al. (2015) as hosted mainly by garnet–pyroxene–epidote skarns and the nearby quartz–epidote rocks. However, the KMC stands out due to its Au-bearing skarn mineralization. In particular, we shall discuss the much debated question as to whether the Oligocene–Miocene intrusions of the SMMMB can be followed into the Rhodope Massif and to the Cassandra ore district and whether these intrusions represent the back-arc magmatism with respect to the occurring Pb–Zn–Au deposits, or alternatively, whether they are related to the post-orogenic collapse of an overthickened crust in the internal Dinarides

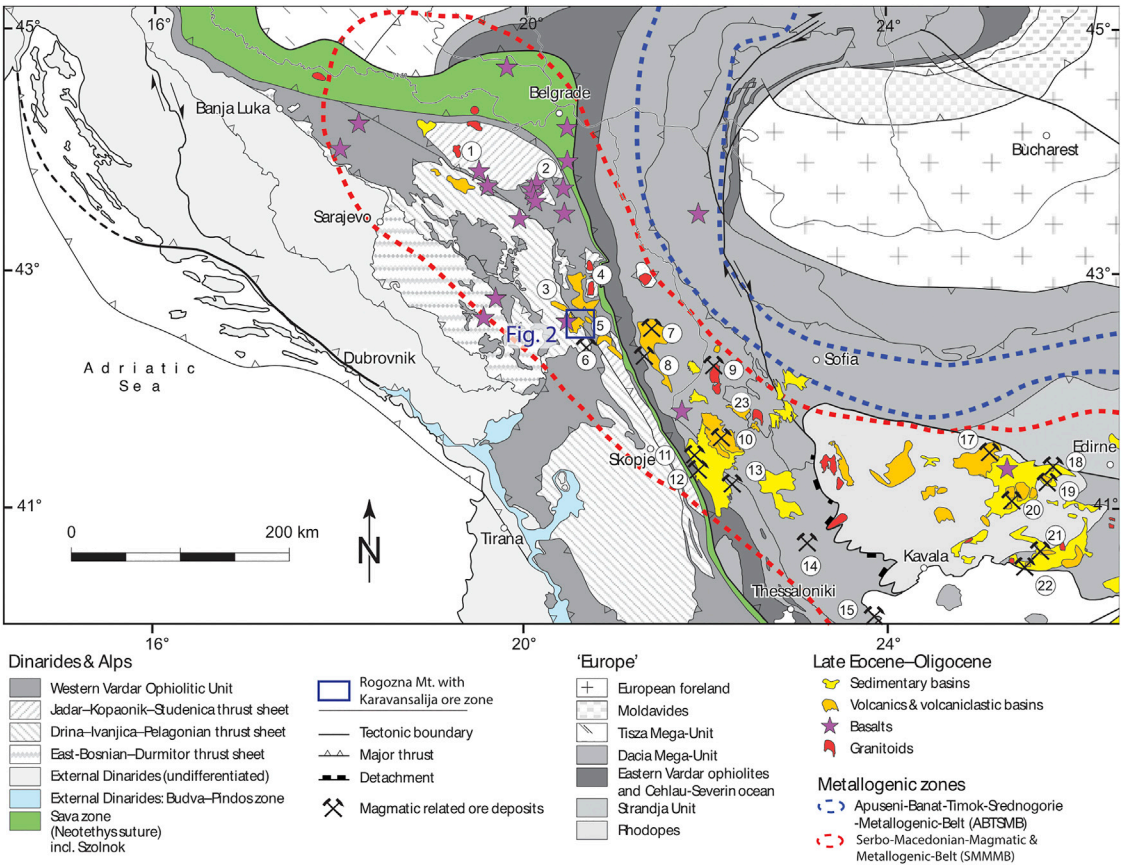

FIGURE 1 | Simplified overview of the major units of SE Europe after Schefer et al. (2010a) and Schmid et al. (2020) with the location of the Karavansalija Mineralized Center (KMC) area indicated by the blue rectangle. The distribution of the Cenozoic magmatism is shown in yellow (sediments), orange (volcanics), and red (intrusives); purple stars mark the position of basaltic rocks. **Table 1** refers to the main Cenozoic deposits displayed here with numbers. The insect locates the position of **Figure 2**.

(Koroneos et al., 2010), mantle delamination, and/or to the extension in the Pannonian basin (e.g., Cvetković et al., 2007).

These coupled data from the KMC base-metal deposit allow us to resolve the chemical evolution and the changing physical state of the magma reservoir over time and the timescales of hydrothermal processes.

REGIONAL GEOLOGY

The Western Tethyan magmatic belt, whose remnants occur today in SE Europe, can be traced through the countries of Slovakia, Hungary, Romania, Serbia, Kosovo, northern Macedonia, Greece, and Bulgaria (**Figure 1**). The magmatic belt is known as one of the Europe's most significant ore-bearing belt including Cu–Au and Pb–Zn–Ag metal deposits. The tectonic setting and geodynamic evolution along the 3,500-km strike of the Western Tethyan belt are complex and broadly evolved from the Upper Jurassic to the Late Cretaceous (Gallhofer et al., 2015). Along the Sava suture zone, subduction-related arc magmatism including locally extensional-related magmatism was fairly minor until the Eocene (Ustaszewski et al., 2010; Stojadinovic et al., 2013; Gelder et al., 2015; Stojadinovic et al., 2017; Toljić et al., 2018); the reactivating of magmatism during the early Eocene (<42 Ma) probably started with the transitioning from collision to post-orogenic extension (late Eocene to early Oligocene) and a further widespread extension-related magmatism during the Miocene (Seghedi et al., 2004; Richards, 2015). This resulted in the formation of the late Eocene to Oligocene sedimentary basins, volcanic centers of calc-alkaline, high-K calc-alkaline, and shoshonitic composition, and extension-related epithermal deposits that formed between 30 and 35 Ma (Moritz et al., 2014, **Figure 2**). The Late Cretaceous Apuseni–Banat–Timok–Srednogorie belt (ABTS belt) (von Quadt et al., 2005; Gallhofer et al., 2015) is dominated of Cu-rich deposits, with a total endowment of ~20 million tons (Mt) of Cu compared to ~15 Mt of Cu deposits in the Cenozoic, whereas the Cenozoic porphyry deposits contain the largest concentration of the Au content (63.6 Moz) (Baker, 2019). Furthermore, there are a few major economic high-sulfidation epithermal deposits directly associated with porphyry deposits in the Cenozoic. The Cenozoic Au ± Cu deposits span greater ranges in age, distribution, and style than the Cretaceous deposits (Baker, 2019; Marchev and Singer 2002; Marchev et al., 2010). In a very simplistic view, the age variation of the Cenozoic deposits show several clusters at 35–31 Ma, 28–24 Ma, 15–12 Ma, and <9 Ma

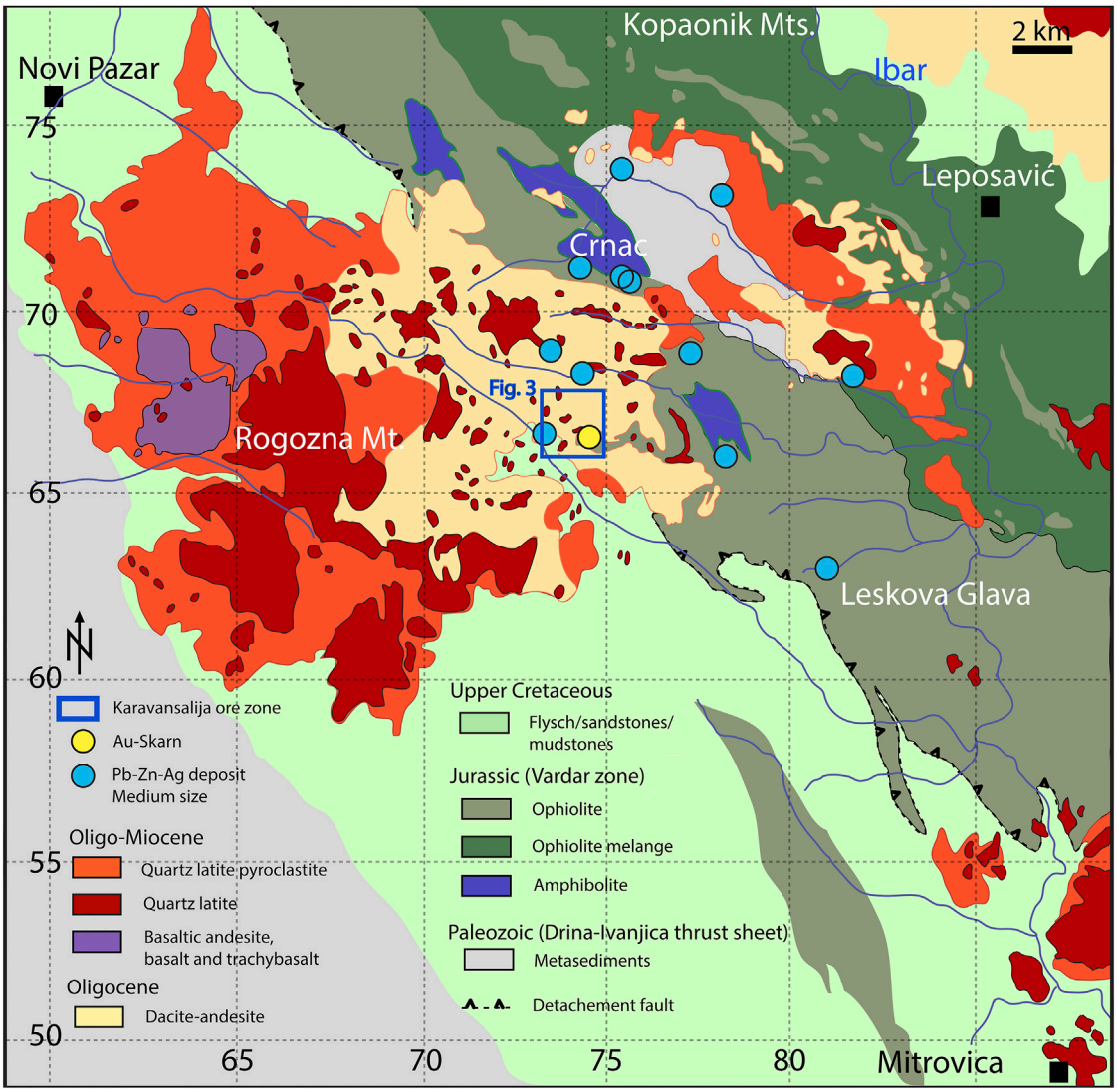

FIGURE 2 | Geologic map of the Rogozna–Kopaonik mountain areas with the location of the Karavansalija Mineralized Center (KMC), highlighted by a blue square (modified after Urošević et al., 1973 and Borojević Šoštarić et al., 2012). The location of the most important medium-sized base metal deposits Crnac and Leskova Glava are shown.

(Baker, 2019) in comparison to the Cretaceous age cluster with its Cu–Au deposits between 92 and 80 Ma (von Quadt et al., 2005; Jelenković et al., 2016; Banješević et al., 2019).

The central Balkan Peninsula is characterized by a complex geotectonic framework which mainly developed during Mesozoic convergence and collision processes. There is a general agreement that the Tethys finally closed during the late Mesozoic and that the West Dinarides and the East Vardar units represent relicts of former oceans. The Serbo-Macedonian magmatic and metallogenic belt (SMMMB, **Figure 1**) represents one major part, traditionally been considered as the Pb–Zn–Bi–Ag–Au dominant ore district in Cenozoic time (Janković, 1997; Borojević Šoštarić et al., 2012). The occurring Cenozoic granitoids associated with ophiolites provide important constrains on the geodynamic setting. The Late Eocene to earliest Miocene magmatic activity is widespread in the Dinarides and is thought to be related to rollback and possibly slab break-off of the Adriatic/African plate (**Figure 1**) (Andrić et al., 2018). The Eocene to Oligocene core complex formation as observed in the Kopaonik area is abundant in the Dinarides and well documented (**Table 1**) for the northern Bosnia, Cer, Bukulja, Fruška Gora, and Jastrebac areas (Ustaszewski et al., 2010; Matenco and Radivojević, 2012; Stojadinovic et al., 2013; Toljić et al., 2013; Mladenović et al., 2015; Erak et al., 2017) and the Central Rhodopes (Marchev et al., 2005; Rohrmeier et al., 2013). Published geochronological data (**Table 1**) of the Rogozna Mt. magmatic rocks allow for distinguishing two main magmatic events: 1) the andesitic to dacitic volcanics occur in the eastern part of the Rogozna Mountain magmatic complex with Ar/Ar ages of ~30 Ma and 2) the quartz-latites lasted from 29.5 ± 0.1 to

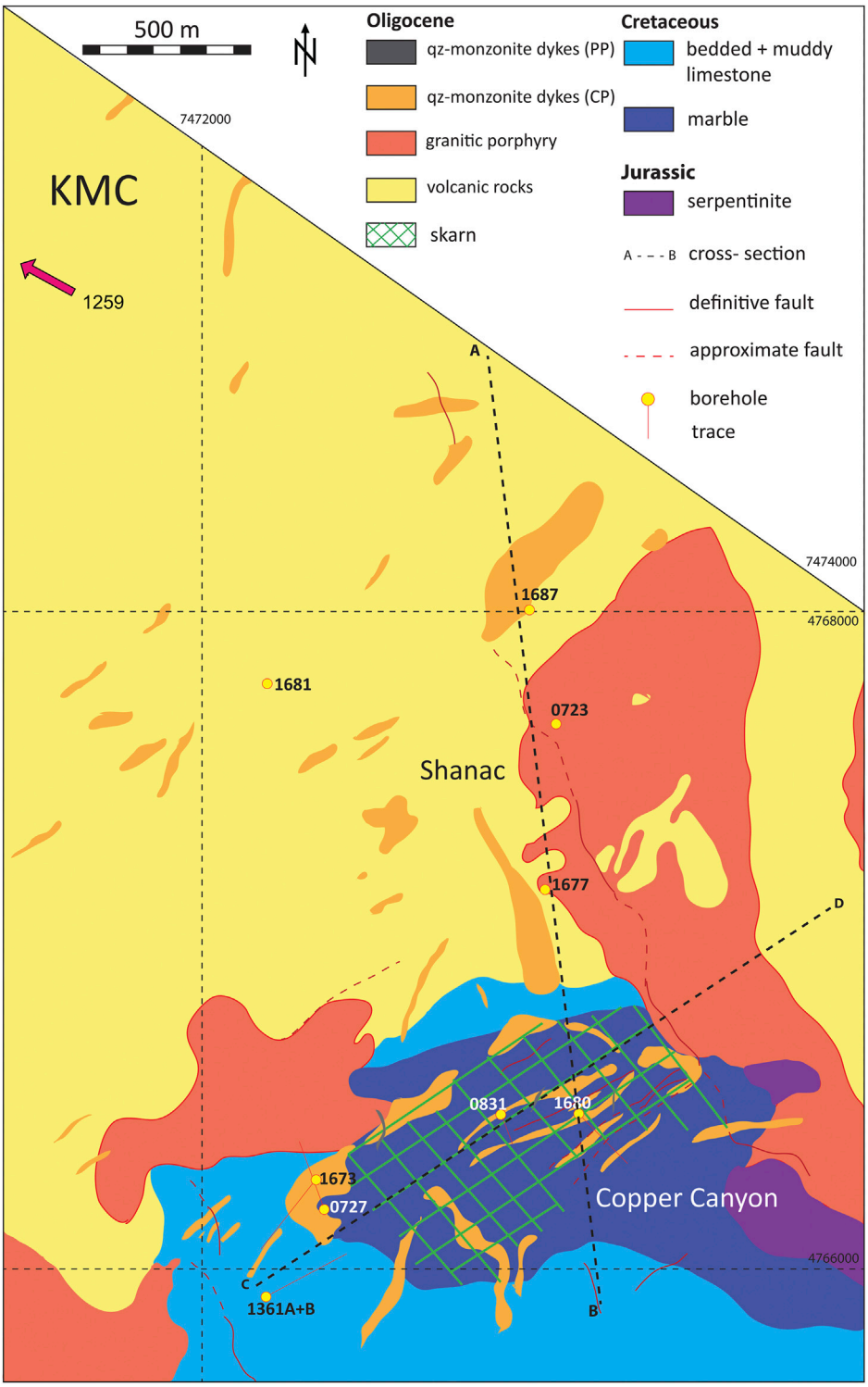

FIGURE 3 | Geological map of the Karavansalija Mineralized Center (KMC) with the location of two profiles AB (Shanac area) and CD (the Copper Canyon) modified after Euromax Resources Ltd. The drill holes used for dating are marked with yellow dots. Dacite = 1,687, quartz–latite = 1,259 (lies about 6 km northwest of the Shanac area, see red arrow), granite = 1,677, quartz–monzonite = 0,727, granite (CP) = 0,723, quartz–monzonite = 1361A, and quartz–monzonite (PP) = 0,831, 1361B, syenite = 1,681. Quartz–monzonites = 1361B, 1,673, and 1,680 are drill-holes used for other purposes than dating.

TABLE 1 | Summary of published geochronological data of Late Eocene to Oligocene magmatism.

Ore deposits related to the Late Eocene to Oligocene magmatism

	Deposit/intrusion	Country	Deposit type	Associated volcanics	Metals	Age in Ma	Method	References
1	Veliki Majdan	Serbia	—	Ultrapotassic lamproites	—	33.5 ± 1.28	K/Ar	Prelević et al. (2004)
2	Rudnik	Serbia	Vein type Pb/Zn	Quartz latite	Pb, Zn, Ag	22.99 ± 0.28	U/Pb	Cvetković et al. (2016)
3	Golija	Serbia	Contact meta., skarn-related	Granodiorite to quartz–monzonite	Pb, Zn, W	20.58–20.17	U/Pb	Schefer et al. (2011)
4	Kopaonik and Željin	Serbia	No deposit	Quartz-diorite, quartz–monzonite	—	31.77–30.7	U/Pb	Schefer et al. (2011)
5a	Karavansalija	Serbia	Au skarn	Quartz latite to latite	Au ± Cu-Pb-Zn	27.76 ± 0.013 to 27.62 ± 0.01	U/Pb	This work
5b	Crnac	Serbia	Vein type Pb/Zn	Quartz latite	Pb, Zn, Ag	29.5 ± 0.1 to 27.3 ± 0.1	K/Ar	Borojević-Šoštarić et al. (2012)
6	Trepca	Kosovo	Breccia pipe and skarns, stratiform mantos	Phreatomagmatic breccia, quartz latite	Pb, Zn, Ag (Ag)	25.1 ± 0.9 to 23.2 ± 0.7	K/Ar	Strmić (2016)
7	Lece	Serbia	Breccia pipe and skarns, stratiform mantos	Volcanoclastics	Pb, Zn, Ag (Ag)	32–28	K/Ar	Pamic and Balen (2001)
8	Kiseljak	Serbia	Porphyry–Cu–Au	Andesite	Cu, Au	23–12	K/Ar	Serafimovski et al. (2010)
9	Surdulica	Serbia	Porphyry–Mo	Granodiorite to monzonite		33–29	K/Ar	Ćebić (1990)
10	Kratovo–Zletovo	Macedonia	Porphyry–Cu–Au	—	Pb, Zn, Ag (Ag)	26.5	—	Serafimovski and Boev (1996)
11	Buchim–Damjan–Borov Dol	Macedonia	Porphyry–Cu–Au, Skarn	Gneiss, andesite	Cu, Au, (Ag), Fe	24.5–24.0	U/Pb	Lehmann et al. (2013)
12	Ilovica	Macedonia	Porphyry–Cu–Au	Granodiorite-porphyry	Cu, Au, (Ag)	30.31–30.12	U/Pb	Georgiev et al. (2012)
13	Jekario	Greece	Porphyry–Cu–Au	—	Cu, Au (Ag)	34–22	—	Frei (1992)
14	Vathi	Greece	Porphyry–Cu–Au	Rhyodacite	Cu, Au (Ag)	18 ± 0.5, 17 ± 1	U/Pb	Frei (1992)
15	Stratoni	Greece	Porphyry	Granodiorite porphyry	Cu-Au	24.5 ± 0.3	U/Pb	Siron et al. (2016)
16	Skouries	Greece	Porphyry–Cu–Au–PGE	Granodiorite porphyry	Cu, Au, PGE	19.6 ± 0.2	U/Pb	Siron et al. (2016)
17	Spahievo	Bulgaria	Volcanic-hosted intermediate sulfidation	Volcanoclastics	Pb, Zn, Cu, (Au–Ag)	34.5–31.76	—	Singer and Marchev (2000)
18	Lozen	Bulgaria	Volcanic-hosted intermediate sulfidation	Volcanoclastics	Pb, Zn, Cu, (Au–Ag)	36.5–35	K/Ar	Lilov et al. (1987)
19	Madjarovo	Bulgaria	Volcanic-hosted intermediate sulfidation	Volcanoclastics	Pb, Zn, Cu, (Au–Ag)	32.7–32.2	^{40}Ar/^{39}Ar	Singer and Marchev (2000)
20	Pcheloyad and Zvezdel	Bulgaria	Volcanic-hosted intermediate sulfidation	Volcanoclastics	Pb, Zn, Cu, (Au–Ag)	31.9–31.1	^{40}Ar/^{39}Ar	Marchev et al. (2004)
21	Sappes	Greece	Volcanic-hosted high sulfidation	Volcanic and intrusive	Cu, Au (Ag)	33.5–19.6	K/Ar	Pecskay et al. (2003)
22	Perama and Maronia	Greece	Volcanic-hosted high sulfidation	Sandstones and volcanics	Cu, Au (Ag)	<29.8–28.7	—	Marchev et al. (2013)
23	Kopriva	Bulgaria	No deposit	KF-granite	—	31.89 ± 0.25	U/Pb	Hörler, J. (2014)
24	Ruen	Bulgaria	Dyke	Trachy-rhyodacite	Pb-Zn-Cu	28.63 ± 0.58	U/Pb	Grozdev et al. (2017)

27.3 ± 0.1 Ma (Borojević Šoštarić et al., 2012). The process of roll-back of the subducted oceanic crust in the Carpathians and the Aegean area (Rhodope Massif) induced local clockwise rotation of the Dinarides and caused the sharp bend of the Sava suture zone south of Belgrade in map view (**Figure 2**) as documented by paleomagnetic studies (Lesić et al., 2019).

This region has been traditionally considered as a Pb–Zn–Ag dominant district (Janković, 1997; Borojević Šoštarić et al., 2012), but in fact, it has a large Au endowment (~25 Moz; (Baker, 2019), as well. Gold is associated with a number of Oligocene–Miocene porphyries (Skouries, Illovitza, Buchim, and Tulare) and carbonate replacement deposits (Olympias and Piavitsa), as

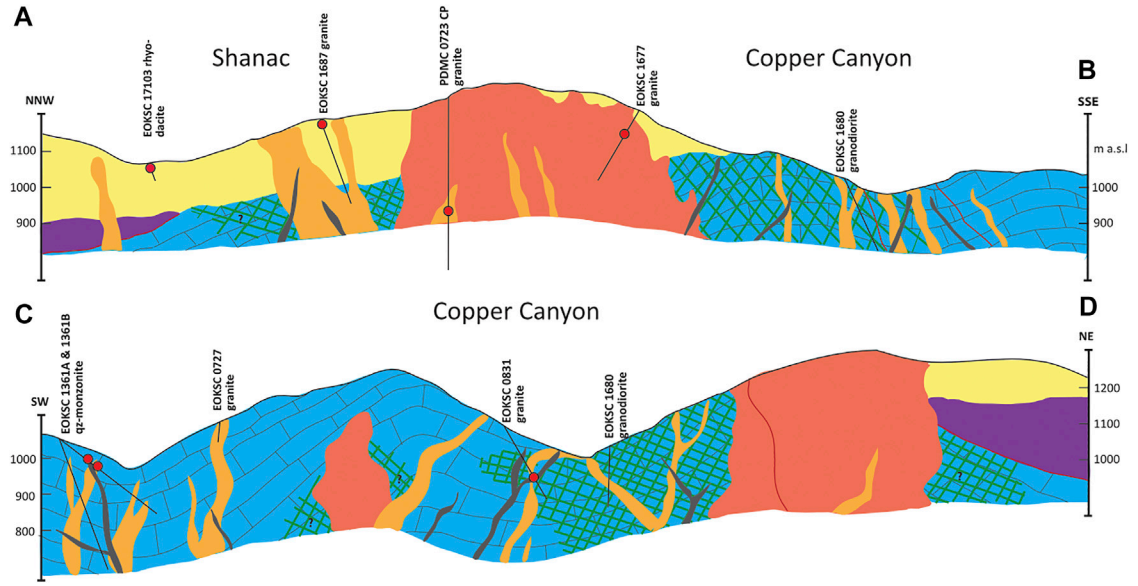

FIGURE 4 | Schematic geological profiles of the KMC region (AB and CD on **Figure 3**; the legend as on **Figure 3**). The red dot on each individual trace of the drill hole marks the location of the selected sample.

well as with the Plavica high-sulfidation epithermal deposit. Notable are the Trepča Pb–Zn deposit in Kosovo with still 60 million tons of ore reserves left; the Lece district in southeastern Serbia with its epithermal gold mineralization (Pamic and Balen, 2001); the Perama Hill high sulfidation Au–Ag–Te–Se deposit in northeastern Greece hosted in altered volcanic rocks; and Skouries, the high grade Au–Cu porphyry deposit in northern Greece (Melfos and Voudouris, 2017; Voudouris et al., 2019).

Geology of the Karavansalija Mineralized Center (KMC)

The KMC is subdivided into three mineralized areas called Shanac, Gradina, and Copper Canyon (**Figures 3**, **4**). The most dominant lithology on the surface is represented by volcaniclastic rocks that correspond to the earlier stage of the Cenozoic magmatism. Shallow-intrusive bodies and dykes of probably the Cenozoic age intrude the volcanic and sedimentary rocks. The skarns are mainly exposed in the southern part (**Figures 3**, **4**) of the KMC, and they are described as products of metasomatic alteration (Urosević et al., 1973). The Upper Cretaceous limestones reacted with the intruding of shoshonitic extrusive rocks during the last stage of the Oligocene–Miocene volcanism, and they are composed of epidote, grossular, zoisite, calcite, pyroxene (hedenbergite), and rarely quartz. Proximal garnet, diopside, epidote ± wollastonite, followed by a pyroxene–epidote zone with subordinate garnet skarn mineral composition and distal skarnized limestone with dominant epidote and occasional pyroxene are described by Dusanić (2006; citation in Budinov et al., 2015).

The KMC was mentioned as an occurrence of gold–copper mineralization with secondary base-metal enrichments, which is distal to known deposits in the Rogozna Mountains (Urosević, et al., 1973; Kandic et al., 1987). The ore mineralization is described by Budinov et al. (2015). It is hosted mainly by garnet–pyroxene–epidote skarns and the nearby quartz–epidote rocks and the overlying volcanic and volcaniclastic rocks. Disseminated cobalt–nickel sulfides from the gersdorffite–krutovite mineral series, cobaltite, and pyrite–marcasite–chalcopyrite–base metal aggregates are defined in the epidosites. The skarn sulfide mineralization is characterized by chalcopyrite, pyrite, pyrrhotite, bismuth-phases (bismuthinite and cosalite), arsenopyrite, gersdorffite, and sphalerite (Budinov et al., 2015). Arsenopyrite aggregates with subordinate amounts of pyrite and chalcopyrite have been described in the overlying volcaniclastic rocks. Gold is rarely developed in visible aggregates of native gold but occurs mainly "invisible" in arsenopyrite. Fluid inclusion micro-thermometry with homogenization temperature in the range of roughly 150–400°C and varying salinities (0.5–8.5 wt% $NaCl_{eq}$ for two-phase low-density fluid inclusions and 15–41 wt% $NaCl_{eq}$ for two- and three-phase high-salinity fluid inclusion) are interpreted as evidence for two fluid sources of the Cu–Au mineralization—magmatic and meteoric. The primary magmatic source of mineralizing fluids is confirmed by sulfur isotope data ranging from 0.4‰ to +3.9‰ $^{\delta}34S_{CDT}$ in arsenopyrite, chalcopyrite, pyrite, and marcasite from the different sulfide assemblages (Budinov et al., 2015).

Relationships of Skarn, Hydrothermal Alteration, and Ore Mineralization

The KMC Cu–Au skarn deposit is a result of the multiphase hydrothermal activity caused by discrete magmatic pulses. The reaction products of skarnitization mainly occur in the Copper

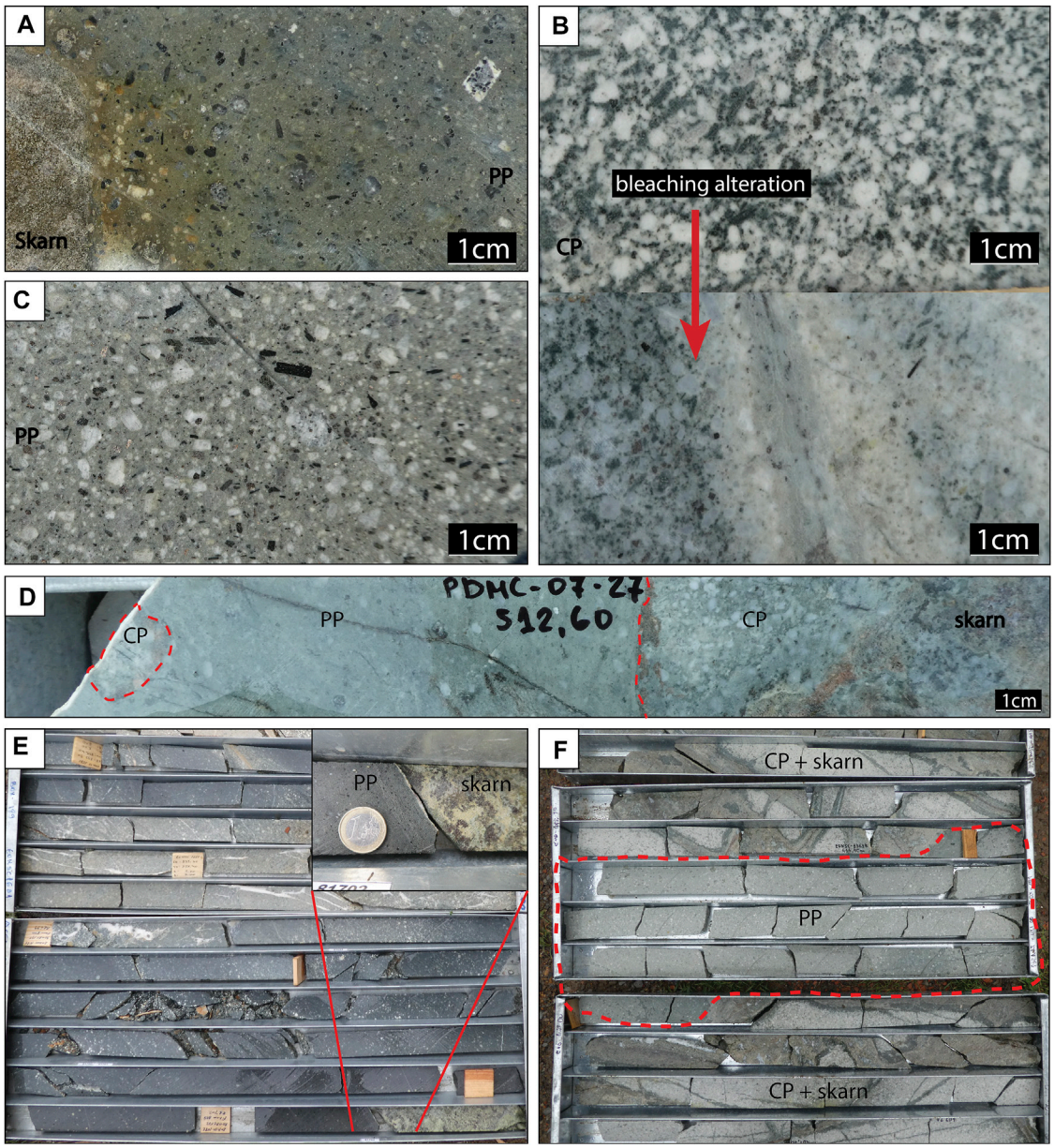

FIGURE 5 | Drill cores of KMC: (for abbreviations see the text) **(A)** EOKSC 0831 PP contact to skarn. **(B)** EOKSC 1680 CP dyke; upper part relatively fresh with feldspar and green patchy areas of altered amphibole and biotite; lower part shows the same rock after the "white" alteration took place, further described in section "*Relationships of skarn, hydrothermal alteration and ore mineralization*", **(C)** EOKSC 0831 PP dyke in skarn, relatively fresh amphiboles, one sanidine phenocryst. **(D)** Drill-core slab of PDMC 0727 with a CP clast in PP and contact to skarnized CP. **(E)** Drill-core section of EOKSC 1681 with a PP-intruding massive skarn on sharp contacts. **(F)** Drill-core section of EOKSC 1361B with a PP-cutting endoskarnized CP.

Canyon (**Figures 3**, **4**); they are observed within the contact zone between the granitic porphyry (e.g., EOKSC 1677) and the Cretaceous limestone (**Figures 5A, D, E, F**). Endoskarns and exoskarns are distinguished at the KMC (in the porphyries and the limestones, respectively). Garnet is the dominant rock-forming constituent of the extensive exoskarns, appearing as relatively small (≤1 mm) grossular crystals. Insights from SEM-EDS (Burkhard, 2017) suggest that the primary garnet belongs to the grossular–andradite solid solution. It may be observed as the "atoll garnet" (Galuskina et al., 2007; Taghipour et al., 2013)—turbid to almost opaque cores of garnet grains, due to fracturing and replacement, with rather clear unaffected rims (**Figures 5A, C**). Common associates of the grossular garnet in exoskarns are grains of hedenbergite, clinopyroxene, and epidote. Corrosion of the garnets and formation of chlorite and/or epidote highlight the retrograde overprint of the garnet skarn. Moreover, calcite is abundant as an interstitial phase between garnet grains but also in fractures through the garnets. In some samples, e.g., EOKSC

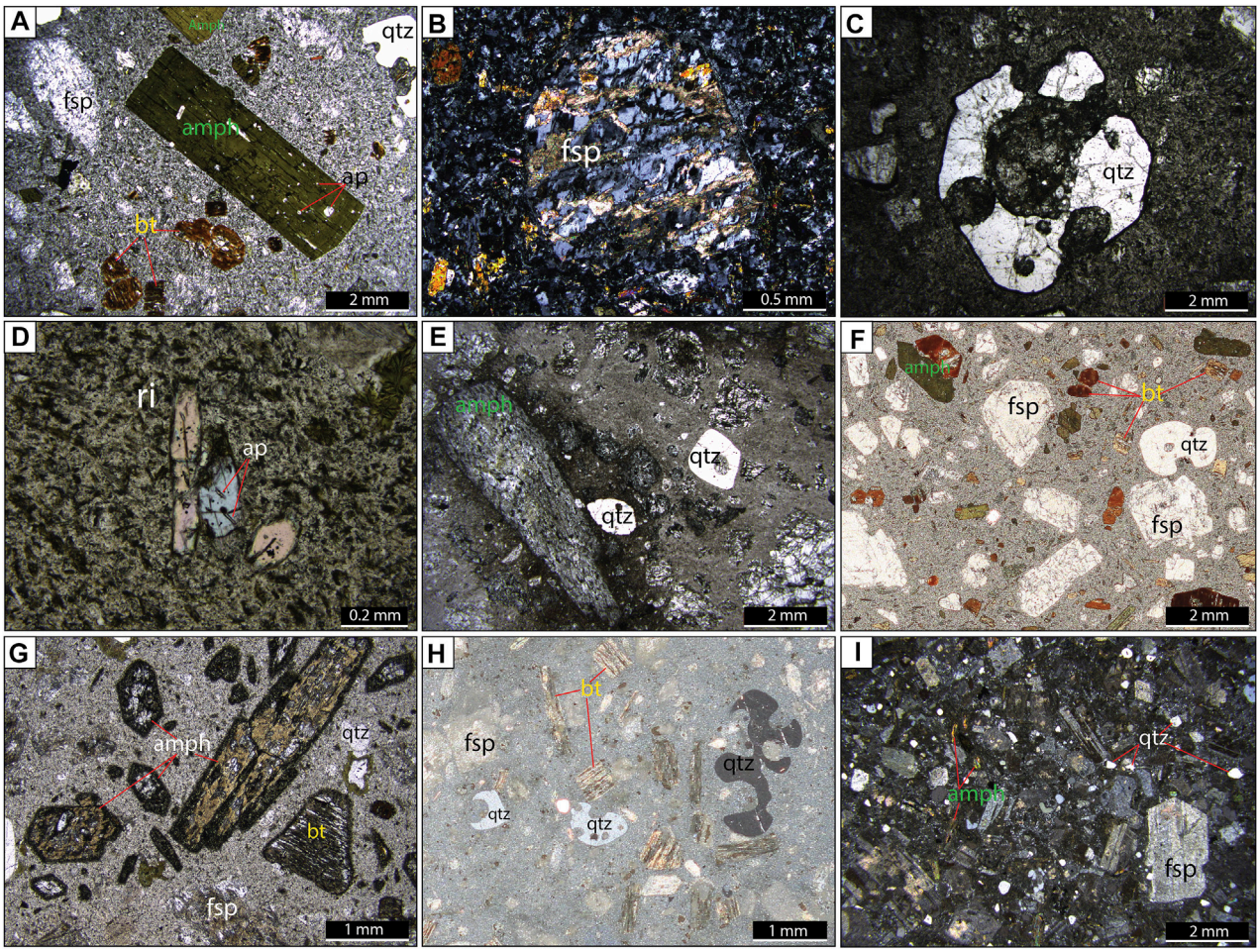

FIGURE 6 | (A) EOKSC 0831 131.1 m (quartz–monzonite, PP) with a big amphibole phenocryst, partly chloritized biotite, quartz with resorption bays, and abundant apatite inclusion in amphibole and biotite. **(B)** Feldspar partly turned to calcite of EOKSC 1361A 445.2 m (quartz–monzonite, PP). **(C)** EOKSC 1673 479.6 m (granodiorite, PP) with a typical big and strongly resorbed quartz phenocryst. **(D)** Diopside in EOKSC 1361A 170 m (quartz–monzonite, PP) with apatite needles as inclusions. **(E)** EOKSC 1680 409 m (granodiorite, CP) showing a strongly altered amphibole to epidote, chlorite ± opaque. **(F)** EOKSC 0727 227.4 m (granodiorite, CP) with the freshest minerals of all samples containing intact amphibole, biotite, and feldspar. **(G)** EOKSC 1259 237.5 m (quartz-latite, CP) displaying a strong opaque reaction rim around amphibole and biotite; feldspar partly turned to calcite. **(H)** EOKSC 1677 104 m (granite, CP) strongly phyllic altered with resorbed quartz and chloritized biotite. **(I)** EOKSC 1687 9.2 m (dacite) moderately altered with lots of feldspar and some amphibole and small quartz grains.

1361A, 182 m (**Figure 5E** , **Figure 6C**), in a strongly base-metal–mineralized dark-green to black rock mass, ilvaite was found as a dominating alteration mineral. The latter is considered a retrograde skarn mineral replacing garnet and clinopyroxene (Burt, 1989). Fe-rich axinite occurred as a vein constituent along with quartz and calcite (EOKSC 1361A, 51 and 164 m; **Figure 5B**). The first intrusion of the granitic porphyry shows itself a phyllic overprinting, i.e., feldspars, amphiboles, and biotite have all been altered to sericite and minor quartz (observed at EOKSC 1677, 104 m). This hydrothermal alteration along with the extensive skarnitization field, prograde, and retrograde mineral associations provides evidence for high syn-to post-intrusion fluid activity which would be required for extensive metasomatism.

Intrusions of the "crowded" quartz-monzodioritic porphyry (CP; description in next chapter 3) discretely cut through the exoskarn, proving that CP is younger than the latter. However, the porphyry is itself prone to strong skarn reactions along fractures/veins. Although the contacts of this porphyry to the exoskarns are typically clear, intrusive juxtaposition of those chemically very different lithologies did not leave the intruding porphyry unaffected (**Figures 5C, D, F**). Bleaching (**Figure 5B**) associated with weak (i.e., incipient) skarn reactions is observed. Endoskarn veins contain garnet, but the abundance of epidote and, especially, chlorite and calcite points to a generally retrograde skarn characteristic.

In endoskarns, incipient reactions in porphyries could be recognized as the matrix taking a turbid greenish hue in haloes around thin (≤1 cm) skarn veins, or along contacts to the exoskarn. The coloring effect is accompanied by mineral reactions by which plagioclase is replaced by alkali feldspar and amphiboles and biotite are transformed into calcite, minor

TABLE 2 | Sample material.

Sample name	Borehole	Depth in m	QAP classification	Magmatic rock type
EOKSC 17103	17,103	59.4	Granite, rhyodacite	Volcanic rock
EOKSC 1687	1,687	9.2	Granite, rhyodacite	Sub-volcanic rock
EOKSC 1677	1,677	105	Granite	Shallow level intrusive rock
EOKSC 1259-CP	1,259	237.5	Granite/rhyodacite	Volcanic rock
EOKSC 0831-PP	0,831	131.5	Granite	Shallow level intrusive rock
EOKSC 1681-PP	1,681	843.8	Quartz-monzo-diorite	Shallow level intrusive rock
EOKSC 1361B-PP	1361B	223	Quartz–monzonite	Shallow level intrusive rock
EOKSC 1361A-CP	1361A	170.5	Quartz–monzonite	Shallow level intrusive rock
EOKSC 0723-CP	0,723	466	Granite	Shallow level intrusive rock
EOKSC 0727	0,727	41	Granite	Shallow level intrusive rock

clinopyroxene, and alkali feldspar, whereas epidote and calcite precipitate in small amounts along fractures.

The overall volume of CP intrusions remains unspecified; however, they clearly occur as dykes. Thus, they are expected to lack the necessary heat for significantly extending the existing exoskarns field (related to the earlier emplacement of the granitic porphyry). On the other hand, the frequent occurrence of endoskarn sections does prove a hydrothermal event induced by the CP intrusion. All lines of evidence point to the CP intrusion being the pulse that delivers and precipitates ore minerals as the later intrusion of porphyry dykes may reveal weak endoskarn veining but does not cause significant skarnitization (**Figures 5A, C–F**) neither host economic mineralization.

The main ore minerals at the KMC are pyrite, arsenopyrite, pyrrhotite, chalcopyrite, sphalerite, and galena. They are commonly found in exoskarn and endoskarn samples. Magnetite is notably present in EOKSC 1361A (182 m) and 0,831 (340 and 508 m). Hematite was found only in accessory amounts, and there were occurrences of marcasite together with pyrite. Pyrite and arsenopyrite seem to be early phases; they occur along the boundaries of skarn rocks to veins, or alternatively, they have sub-to euhedral shapes in skarn masses. Sphalerite and galena likely appear the latest in the mineralization sequence; pyrrhotite and chalcopyrite are, thus, thought to form before them. However, these sulfide ore phases are often intimately associated with each other, which preclude the identification of a clear precipitation sequence.

The skarn formation with its propylitic and phyllic alteration and the contact relationships between skarns and the different porphyries, skarn veins and mineralization indicate three main phases of hydrothermal activity (Hoerler, J. 2017): 1) formation of extensive prograde exoskarns (garnet skarn) in the sedimentary host rocks, emplacement of a comparably larger subvolcanic granitic intrusion; 2) cooling of the skarn system that leads to retrograde overprinting of the garnet skarn; and 3) intrusion of the quartz-monzonitic porphyry dykes that partly reactivates the skarn system and results in vein-bound mineralization of base metals and, especially Au in exoskarn and endoskarn veins (Burkhard, 2017). Subsequent quartz-monzonitic porphyry intrusion remains unmineralized, but it does also show less pronounced endoskarn veining.

ANALYTICAL METHODS, SAMPLE LOCATION, AND PETROGRAPHIC DESCRIPTION

The details of the methods and sample location are documented in the **Supplementary Figure S1**. All selected samples are listed in **Table 2**, including the number of the borehole, the depth, the QAP classification, and the rock type; the selected samples are shown on a geological map, and the relationship to host rocks is documented in two geological profiles of the KMC target area (**Figure 4B**).

The porphyritic rocks have been split in types according to the visible texture and also their relative timing (**Figure 5**): a more phenocryst-rich ("crowded") quartz-monzonitic porphyry (CP) variety (**Figures 5B, D**) and a quartz-monzonitic porphyry with less phenocrysts ("proper") in a fine-grained matrix (PP; **Figures 5C, E, F**). The phenocrystal content of the quartz-monzonitic porphyries ranges between 45–60% and 20–33%, respectively. Almost all quartz-monzonitic rocks are strongly skarn-altered. The volcanic samples (EOKSC 1687, 17103) consist mostly of feldspar (sanidine), amphibole, biotite, and quartz as finer grains instead of larger and resorbed phenocrysts. The texture is fine-grained, and some flow bands are recognized in the hand specimen.

The porphyritic rocks (CP) EOKSC 1361A and 0,723 and the porphyritic rocks (PP) 1361B, 0,831, and 1,681 (**Table 2**) are classified as quartz-monzonitic, quartz-monzodioritic, and granitic (QAP classification) and appear as dykes of several meters to 100 m in thickness. The main phenocrysts of the PP rocks are quartz, plagioclase, K-feldspar, amphibole, biotite, and sanidine. The PP-type intrusions are less encountered in the drill-cores and show a smaller extent than the CP (**Figure 5**). They are as well strongly altered and bleached (**Figure 5B**). The PP dykes contain phenocrysts of quartz, plagioclase, K-feldspar (sanidine), amphibole, diopside, biotite, and phlogopite; they also contain small diopside clusters and evidence of phlogopitization of biotite and diopside selvages around quartz. The granitic porphyry EOKSC 0727 (LP) is the least altered sample compared to all andesitic and granitic/rhyodacitic porphyries marked consequently as late porphyries-LP, **Figures 9**, **10**; cross-cutting dykes are often strongly bleached in the typical white appearance. The skarnitization occurrence is documented in

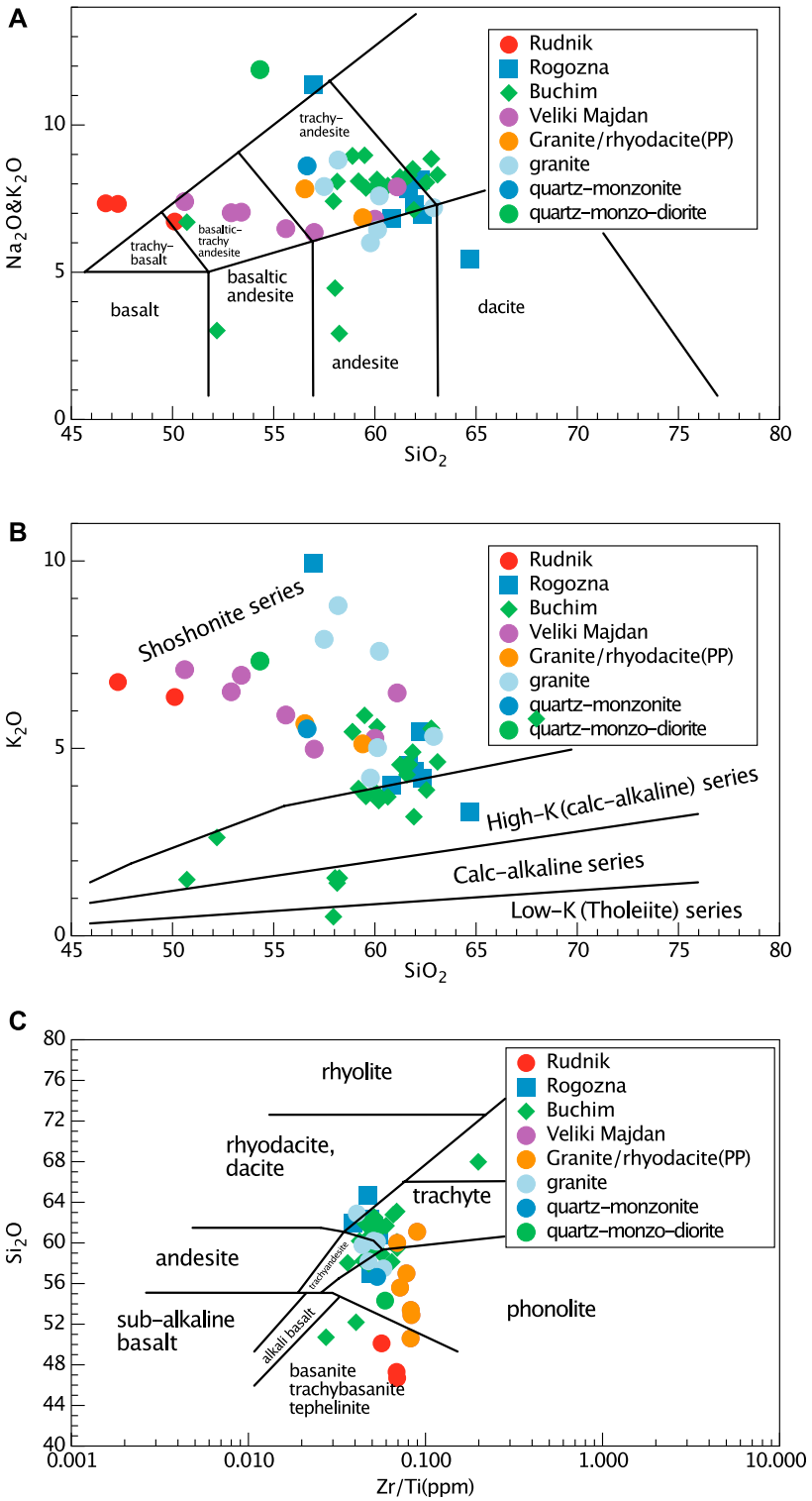

FIGURE 7 | Classification diagrams of whole-rock samples (results from XRF analyses). **(A)** Total alkalis versus silica (TAS) diagram (Le Maitre et al., 1989). **(B)** K_2O versus SiO_2 diagram, boundaries after (Rickwood, 1989). **(C)** SiO_2 versus Zr/Ti (ppm) for altered rocks after (Winchester and Floyd, 1976). Published data used for comparison are from Buchim (Lehman et al., 2013; green diamonds), Rudnik (Cvetković et al., 2006; red circles), Veliki Majdan (Prelevic, 2005; orange circles), and the Rogozna Mts (Borojević Šoštarić et al., 2012; blue squares).

Figures 4–6 between the intrusion contact zone and the marble units; the volcanic rocks on top of the marble and the skarn area in the Shanac area (EOKSC 1677, 1,687, 17103, and 1,259) have a strong sericite–pyrite alteration and replacement of the feldspar into a fine-grained mass of sericite, therefore interpreted as predating the hydrothermal alteration and mineralization.

The knowledge of the geological and temporal relationship of the Eldorado Gold Corporation from field and drill cores and our observations on the relationships of the magmatic rocks to the skarns, hydrothermal alteration, and ore vein were used to select the samples for precise CA–ID–TIMS dating: a phenocryst-rich quartz-monzonitic porphyry (EOKSC 1361A; CP), two apparently younger quartz-monzonitic/granitic porphyries (EOKSC 1361B and 0,831; PPs), a granite porphyry dyke (EOKSC 0727), and a subvolcanic (shallow intrusive body) granite (EOKSC 1677).

RESULTS

Geochemistry of Magmatic Rocks

On the total alkalis vs. silica diagram, the quartz-monzonitic porphyries, quartzz-monzodioritic, and granite/rhyodacite plot in the trachy-andesite field, whereas some granitic rocks are shifted to the andesitic area (**Figure 7A**, **Supplementary Table S3**). All extrusive samples (volcanics) show a trachy-andesitic composition (**Figure 7A**). Available geochemical data of magmatic rocks which are in close relationships to ore deposits, e.g., Buchim (North Macedonia), Rudnik, and Veliki Majdan (Serbia), are of broader compositions, ranging from basaltic-trachy-andesitic to trachy-andesitic and further to andesitic composition (**Figure 7A**); the K_2O vs. SiO_2 plot shows that most samples are of shoshonitic to high-K composition (**Figure 7B**).

To avoid the strong influence of hydrothermal alteration on the rock classification, the discrimination diagram of Winchester and Floyd (1977; **Figure 7C**) was used as it takes the immobile trace elements into account. The majority of intrusive and volcanic rocks of the KMC area plots in the trachy-andesitic, trachytic, and rhyodacitic field, whereas some samples plot into the phonolitic field. However, the latter samples still contain quartz and, therefore, should not be defined as phonolites; they are similar to rocks from Veliki Majdan that represent hybrids of mixing between acid and lamproitic magmas (Prelevic´ et al., 2004). Additional data from other locations with magmatic–hydrothermal ore deposits (Buchim, Rudnik, and Veliki Majdan) from the Cenozoic SMM-MB are plotted on **Figure 7** for comparison and listed in **Table 1**. The results of our study mostly coincide with the ones from the Buchim porphyry (Cu ± Au; (Lehmann et al., 2013), with a slight tendency to a more alkaline, phonolitic composition. Rocks from the KMC area are more silicic and less potassium-rich in contrast to the rocks from Rudnik and Veliki Majdan which mainly plot in the shoshonite series field.

The rare Earth element (REE) patterns show enrichment of light REE (LREE) and depletion of the heavy REE (HREE) with a weak Eu anomaly (**Figure 8A**); the multi-element diagram of the KMC rocks reveals high–field-strength element (HFSE) depletion for Ta, Nb, and Ti, whereas Ba, Sr, and Pb and other large-ion lithophile elements (LILEs), especially U and Th are enriched (**Figure 8B**). These patterns are generally indicative for subduction-related magmatism or for such that is generated in the subduction-modified lithosphere. The plots of La/Sm vs. Yb and Sr/Y vs. Y aim to distinguish between adakite-like and normal arc magmas (**Figures 8C,D**); adakite-like signatures for the ratios La/Sm and Sr/Y higher than 20 and Yb and Y concentration less than 1.9 and 18 ppm are used according to Defant and Drummond (1993) and Richards and Kerrich (2007). The porphyritic dykes of the KMC area (**Figure 7C**) plot on the border between normal arc- and adakite-like affinities. The analyses of the rocks from the Rudnik and Veliki Majdan area mostly plot in the adakite-like field. The intrusive rocks of Buchim and Rogozna show a trend between adakitic to normal arc on higher La/Sm and Sr/Y values. The $(La/Sm)_n$ and $(Dy/Yb)_n$ ratios (**Figures 8E, F**) are used to identify mineral differentiation paths (Davidson et al., 2007; Richards and Kerrich, 2007). The $(La/Sm)_N$ ratio of all samples generally increases with the increasing SiO_2 content (amphibole–garnet fractionation) but shows a slight trend of possible monazite, allanite, or apatite fractionation at SiO_2 of 60% and higher. The $(Dy/Yb)_N$ ratio decreases with increasing SiO_2, which implies amphibole fractionation in all KMC samples. Both diagrams with KMC data show a similar geochemical evolution to those from the Rudnik and Veliki Majdan areas, except the $(Dy/Yb)_N$ rise above 62 wt% SiO_2 in the Rudnik samples, indicating garnet fractionation.

LA–ICP–MS and CA–ID–TIMS Zircon U/Pb Geochronology

The U/Pb LA–ICP–MS data, including $^{206}Pb/^{238}U$, $^{207}Pb/^{235}U$, and $^{207}Pb/^{206}Pb$ U/Pb ratios, are listed in **Supplementary Table S4**, and the obtained data sets are show in **Figure 9**.

The analyzed samples of the KMC show heterogenous zircon population, indicating the existence of inherited zircon population with Cretaceous, Triassic, and Silurian ages (**Supplementary Table S4**); the obtained pre-Cenozoic ages are not plotted but listed in **Supplementary Table S4**. The weighted mean dates of concordant zircons of the LA–ICP–MS study that could be geologically meaningful are plotted in **Figure 9**. All obtained and calculated $^{206}Pb/^{238}U$ ages of the LA–ICP–MS measurements are overlapping within their errors. The calculated 2σ errors of the weighted $^{206}Pb/^{238}U$ ratios are partly less than 0.8%; taking into account the uncertainty of the standard calibration, instability of the laser, and the estimated external error, approximal uncertainties show an approximation uncertainty of 1.5%, which is calculated for each data set (**Supplementary Appendix Figure S2**). For the full data tables, the readers are referred to the **Supplementary Appendix Figure S2**. The presumably older volcanics (17,103, 1,687, 1,677, and 1,259) cannot be distinguished simply based on the LA–ICP–MS data set (**Figure 11**).

The sub-volcanic rocks (**Figure 9**) have an age of 28.56 ± 0.56 Ma and 28.45 ± 0.54 Ma based on two samples (EOKSC 17103 and EOKSC 1687). Two granitic/rhyodacitic porphyries

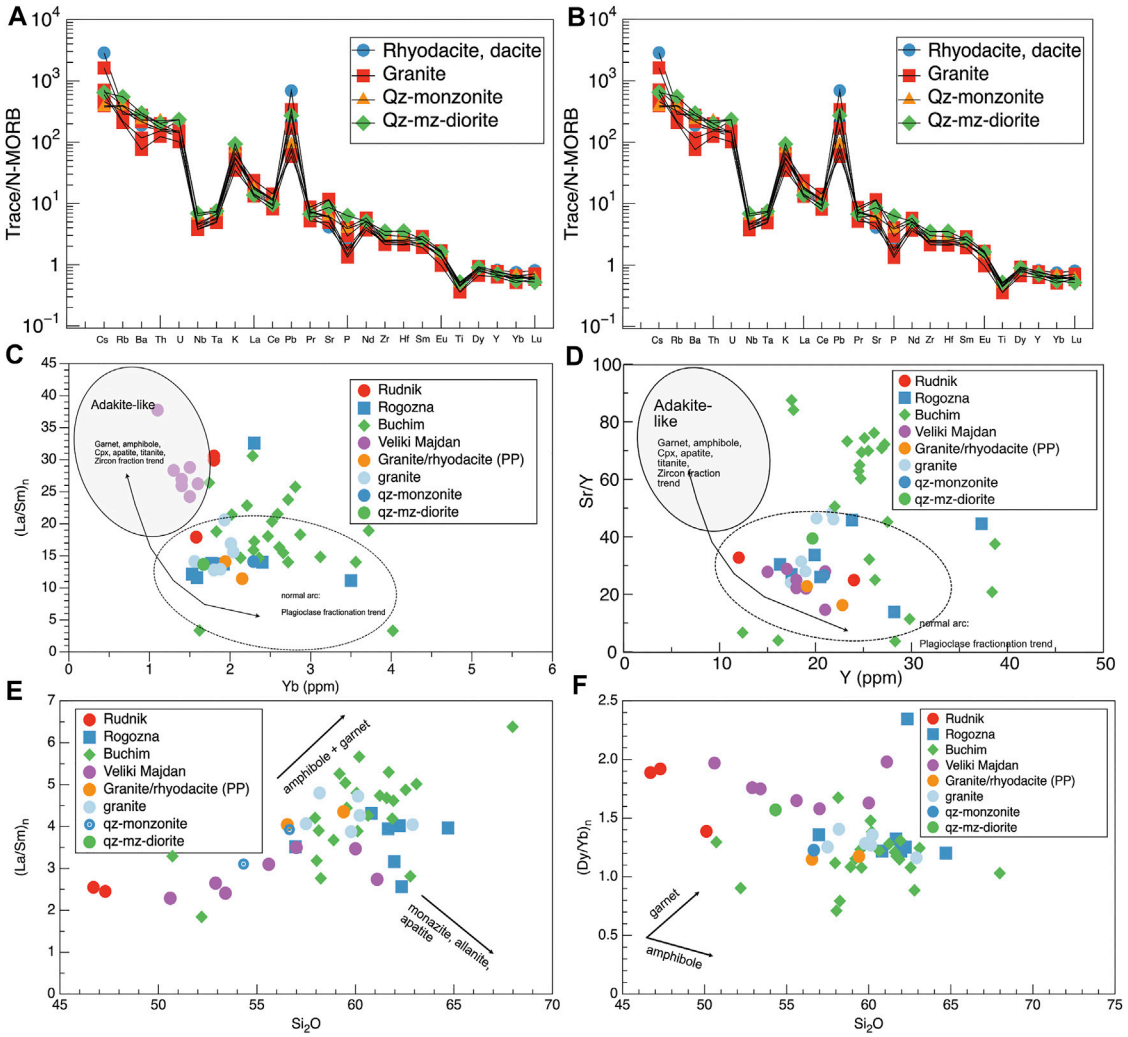

FIGURE 8 | Geochemical diagrams for the whole-rock samples of the KMC: **(A)** and **(b)** REE, trace element, and multi-element spider diagrams normalized to chondrite and N-MORB, respectively (after Sun and McDonough, 1989); **(C)** La/Yb versus Yb (ppm) plot; **(D)** Sr/Y versus Y (ppm) plot; Field for adakite-like and normal-arc magmas from Defant and Drummond (1993), and the qualitative differentiation paths of various minerals from Richards and Kerrich (2007); **(E)** $(La/Sm)_n$ versus SiO_2 and **(F)** $(Dy/Yb)_n$ versus SiO_2 as a measure of fractionation (mineral differentiation paths from Davidson et al., 2007). Published data for other Cenozoic magmatic series as on **Figure 7**.

(EOKSC 1677 and EOKSC 1259) which belong to the older geological unit (Phase I, **Figures 9**, **10**) have weighted mean ages of 28.16 ± 0.53 Ma and 28.49 ± 0.53 Ma. Two pre-ore quartz-monzonitic/granitic dykes (**Figures 9**, **10**) yield ages of 27.35 ± 0.59 Ma and 27.38 ± 0.41 Ma [(Phase II), EOKSC 1361A and EOKSC 0723]. The syn-ore granitic, quartz-monzodioritic, and quartz-monzonitic dykes have ages of 27.47 ± 0.60 Ma, 27.37 ± 0.41 Ma, and 27.42 ± 0.59 Ma based on samples (EOKSC 0831, EOKSC 1681, and EOKSC 1361B, **Figures 9**, **10**), respectively.

One post-ore granitic dyke (PDMC 0727-LP) has a weighted mean age of 26.95 ± 0.40 Ma (MSWD = 1.13). The obtained $^{206}Pb/^{238}U$ ages of the older magmatic group (Phase I, **Figures 9**, **10**) show an overlapping within their uncertainty with the data of the syn- and post-ore formation (**Figure 10**). The obtained dates of Phase I (**Figure 11**), Phase II, ore-formation, and post-ore formation are overlapping although the Phase I with their older mean values indicate a small offset to a previous event.

High-precision CA–ID–TIMS data (**Supplementary Table S5**,) help to resolve the time relationship of rocks and distinguish the presumably older volcanics rhyodacitic/granitic intrusions (Phase I) from the younger quartz-monzodioritic and granitic dykes (phase II) (**Figures 9**, **10**). Zircons of all intrusive and extrusive rocks likely record continuous zircon growth in an evolving magma chamber (Bachmann et al., 2007; Barboni et al., 2013; Buret et al., 2016; Keller et al., 2018). The use of the youngest zircon to determine the age of eruption or magma emplacement has been tested by several studies and accepted in the research approach (von Quadt et al., 2011; Schoene et al., 2013; Wotzlaw et al., 2013; Condon et al., 2015; Buret et al., 2016; Large et al., 2018). This approach of course

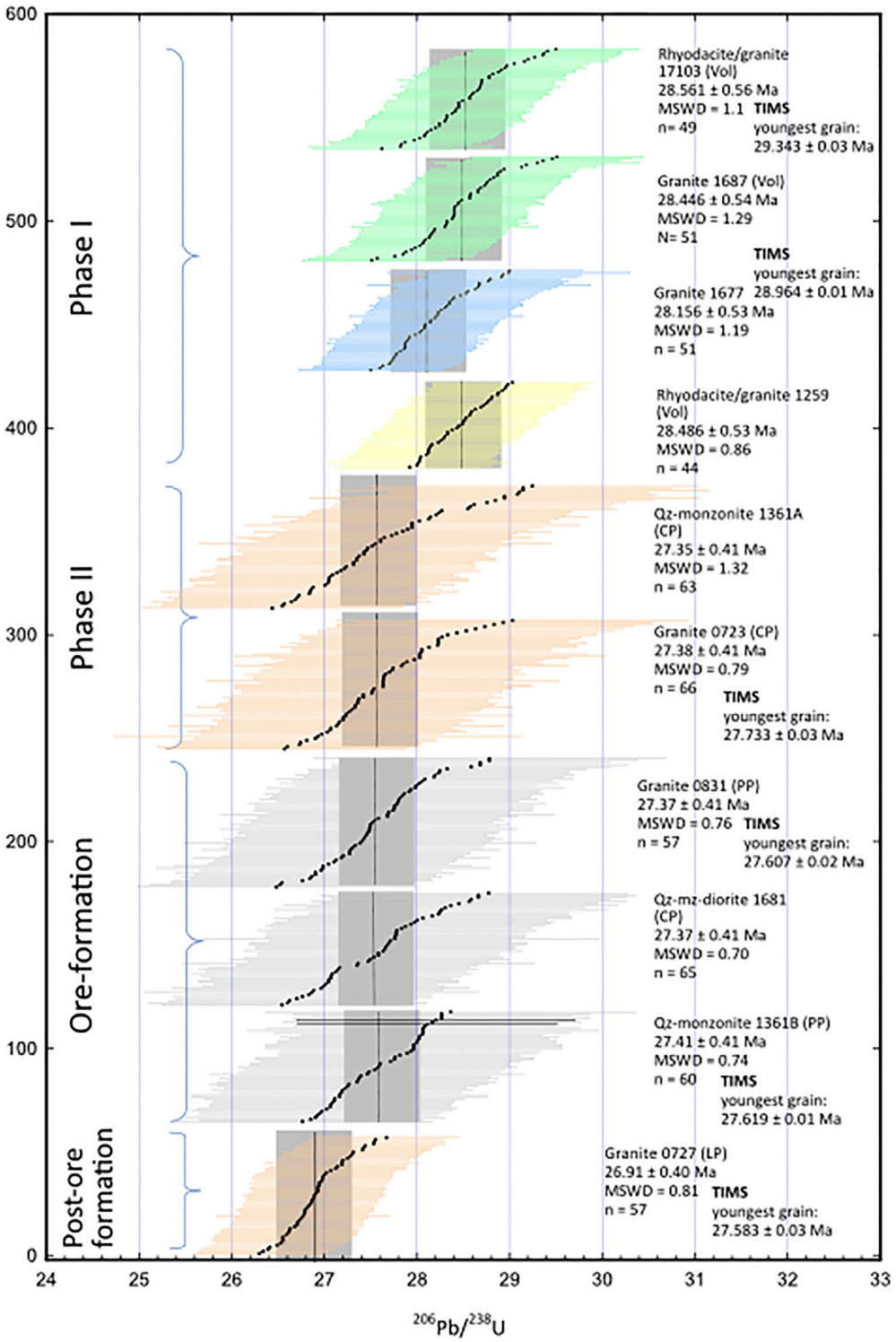

FIGURE 9 | LA–ICP–MS and CA–ID–TIMS age data. Uncertainties reported as 2σ uncertainties. Density plot of LA–ICP–MS data visualized as a thick line over the measurement together with the weighted mean of statistically concordant zircon populations. Systematic uncertainties (external errors) 1.51% (Gehrels et al., 2008; Paton et al., 2010) on weighted means of LA–ICP–MS data included the CA–ID–TIMS dates showing the age of the youngest obtained grain (details **Figure 10**).

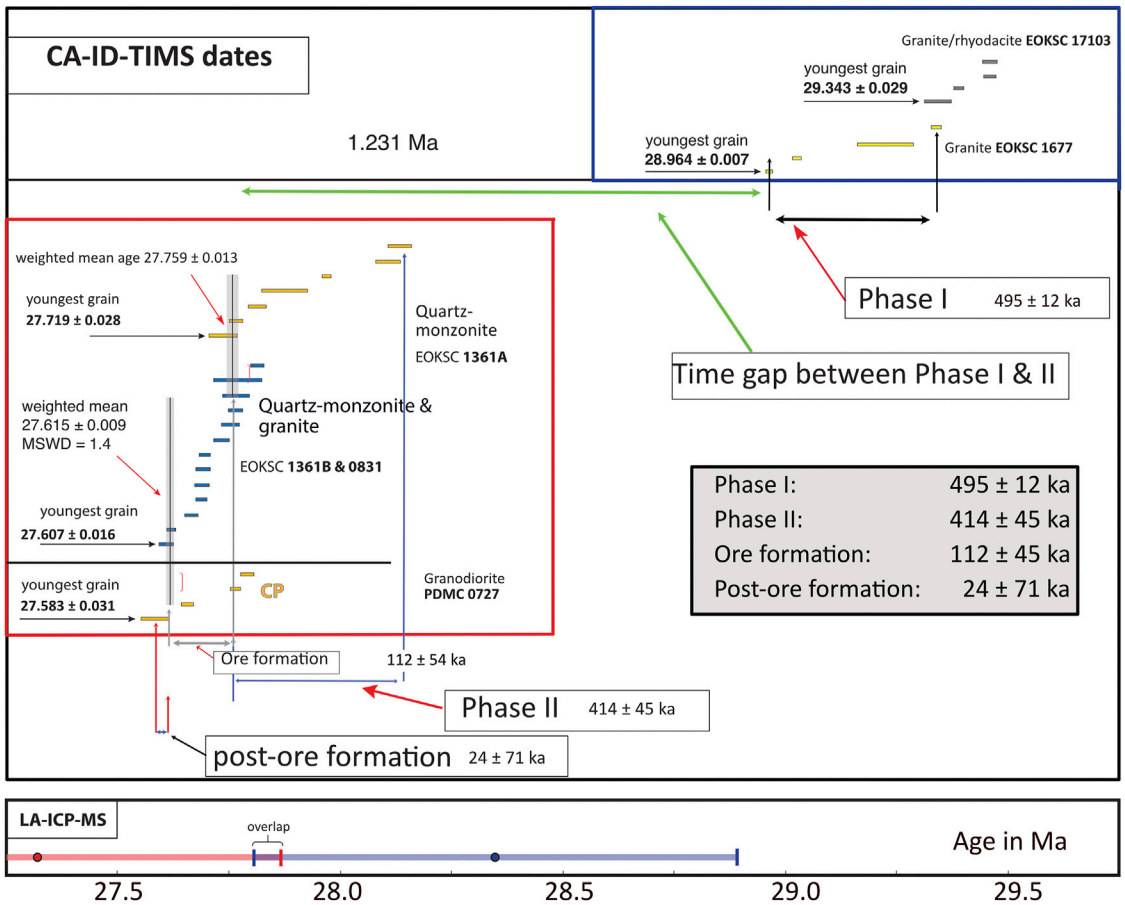

FIGURE 10 | Compilation of high-precision datasets (CA–ID–TIMS) on several pre-, syn-, and post-ore intrusions/extrusions at the magmatic–hydrothermal polymetallic deposit KMC. Phase I with 495 ± 12 ka presents the pre-ore time interval; after a magmatic time gap of 1.231 Ma, Phase II with 414 ± 45 ka is the second pre-ore event and at least the life time of the ore formation with 112 ± 45 ka includes the shortest event at the KMC. The post-ore formation includes a time window of 24 ± 75 ka (EOKSC 07272) Uncertainties are of 2σ confidence interval.

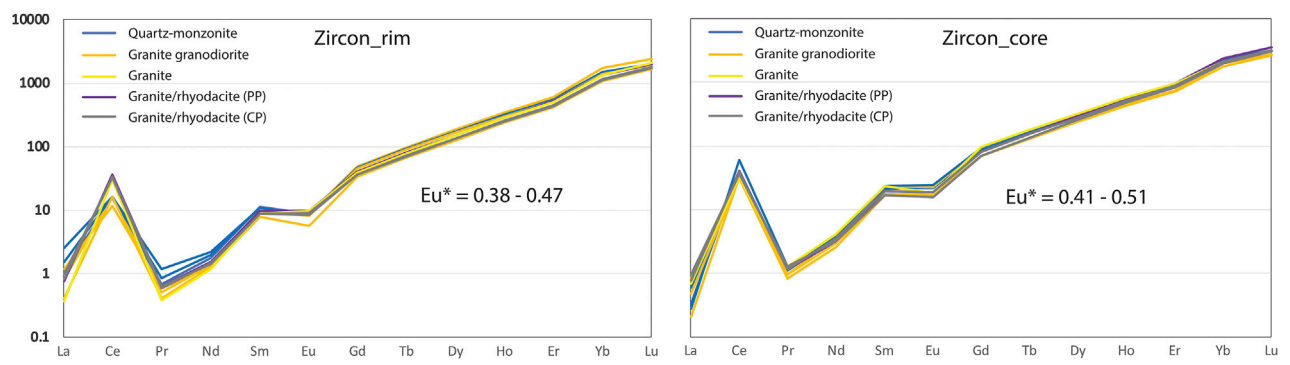

FIGURE 11 | Chondrite normalized (Sun and McDonough, 1989) zircon REE patterns for rim and core crystal parts of the studied samples.

could potentially introduce uncorrected errors (e.g., through zones of Pb-loss on a single zircon grain); this effect, however, should be minimal as the studied zircons are young, and the chemical abrasion technique should be highly efficient.

Several zircon grains of the rhyodacitic-granitic rock (EOKSC 17103, and 1,677) have been selected for TIMS analysis. The youngest zircon age of every sample is regarded as the porphyry emplacement age (Wotzlaw et al., 2013; Szymanowski et al., 2017;

TABLE 3 | Mean 206Pb/238U ages of LA-ICP-MS and CA-ID-TIMS investigation.

Sample	Borehole	TIMS age	LA–ICP–MS age
Rhyodacite	EOKSC 17103	29.343 ± 0.03 Ma	28.56 ± 0.56 Ma
Granite porphyry	EOKSC 1677	28.964 ± 0.01 Ma	28.16 ± 0.53 Ma
Quartz–monzonite porphyry (CP)	EOKSC 361A	27.759 ± 0.013 Ma	27.35 ± 0.41 Ma
Quartz–monzonite porphyry (PP)	EOKSC 361B	27.619 ± 0.01 Ma	27.41 ± 0.41 Ma
Granite porphyry (PP)	EOKSC 0831	27.607 ± 0.02 Ma	27.37 ± 0.41 Ma
Granite porphyry (LP)	PDMC 0727	27.583 ± 0.03 Ma	26.91 ± 0.40 Ma

Keller et al., 2018). The weighted mean LA–ICP–MS ages and the CA–ID–TIMS dates are listed in **Table 3**; further details are available in **Figures 9**, **10** and **Supplementary Table S4**, and **Supplementary Table S5**. The CA–ID–TIMS dates of the granite and volcanics are notably older than the calculated LA–ICP–MS average mean dates (**Table 3**). The discrepancy of U/Pb zircon ages obtained by the CA–ID–TIMS and LA–ICP–MS techniques has been observed at several geological locations (von Quadt et al., 2014; Large et al., 2020; Rottier et al., 2020).

Phase I: The youngest zircon grain (EOKSC 17103) records a date of 29.343 ± 0.03 Ma, and the youngest zircon grain (EOKSC 1677) records a date of 28.964 ± 0.01 Ma (CA-ID-TIMS, **Figure 10**). Phase II: The youngest statistically equivalent zircon grains (n = 2) yield a weighted mean age of 27.759 ± 0.013 Ma (MSWD = 3.4). Ore formation (bracket between the altered and mineralized CP quartz-monzonitic dyke EOKSC 1361A and the PP quartz-monzonitic dykes EOKSC 0831 and 1361B): eight, six, and seven zircon grains of the quartz-monzonitic dykes (EOKSC 1361A), (EOKSC 1361B), and (EOKSC 0831) have been selected for TIMS analysis (**Figure 10**); the youngest zircon records a date of 27.607 ± 0.02 Ma (EOKSC 0831), and the youngest zircons record dates of 27.759 ± 0.013 Ma (EOKSC 1361B), respectively. Post-ore formation: The post-ore granitic porphyry (EOKSC 0727-LP) shows based on the youngest grain an age of 27.583 ± 0.031 Ma (**Figure 10**).

Zircon Trace Element Budget and Hf Isotopes

The analyses of zircon trace element data can be used for distinguishing magmatic pulses on their geochemical characteristics, determine the crystallization temperature, and identify the role of assimilation and fractionation components (Ferry and Watson, 2007; Wotzlaw et al., 2013; Szymanowski et al., 2017).

The REE patterns in zircon are characterized with LREE depletion with respect to HREE together with a weak negative Eu and a strong positive Ce anomaly (**Figure 11**; calculation, **Supplementary Figure S1**). The REE content on zircon rims yields a higher positive Ce anomaly and a slightly weaker Eu anomaly (Eu* = 0.38–0.47) than that on the zircon cores (Eu* = 0.41–0.51; **Figure 11B**). The REE content variations between the samples are not visible or at most seen as slightly higher LREE values (excluding Ce) for the porphyry stock and dykes than all other samples (Hörler, 2017).

Zircon trace element analyses of the granitic, quartz-monzonitic, quartz-monzo-dioritic, and rhyodacitic intrusive/extrusive rocks (EOKSC 727, 1,259, 1,677, 1,687, 17103, 0,831, 1,681, 723, 1361A, and 1361B) have been plotted on **Figures 12**, **13**; the data set is listed in **Supplementary Table S7**. We have used the Th/U, Ce/Sm, Yb/Gd, Ce, Yb, Ti ppm, and Eu-anomaly to demonstrate possible fractionation trends (Halter et al., 2004; Reid et al., 2011; Wotzlaw et al., 2013), mixing mineral fractionation scenario, and crystallization temperature. Several minerals, e.g., apatite, titanite, and allanite have a strong influence by the REE residual melt concentration (Klimm et al., 2008) on the fractionation process in magmatic systems (Szymanowski et al., 2017).

Ti-in-zircon temperatures were calculated using the calibration of Ferry and Watson (2007). For αSiO_2, a value of 1 was used as in all rocks, the quartz occurs as phenocrysts. Ti-bearing minerals are rarely seen in the fresh rock samples, but the trace element patterns propose the presence of titanite as it is also seen in other porphyritic rocks (e.g., in Argentina, Peru, South America) (Chelle-Michou et al., 2014; Buret et al., 2016); consequently, an αTiO_2 of 0.7 was used. Estimated temperatures (zircon rims) for quartz-monzonite, quartz-monzodiorite, and for the granite are low, ranging from 640°C up to about 700°C (**Figures 12G,H**); the estimated zircon core temperature, ranging from 650°C up to 750°C (**Figures 12G,H**). The granite 0,727 (**Figure 12E**) shows a narrow T field between 650 and 670°C, and all rim analyses (EOKSC 0727-LP) show T data below 650°C. A change in the TiO_2 or SiO_2 activity of 0.1 will result in minor differences of ±25°C (including the models uncertainty). These values plot near and probably also below the zircon solidus, similar to other studies on porphyritic rocks (Buret et al., 2016; Chelle-Michou et al., 2014). The role of plagioclase fractionation is visible between rocks of older and younger magmatic evolution; the Eu anomaly (0.4–0.6) of the quartz-monzonite and other sub-volcanic rocks drops down to values <0.4 of the post-ore–related rocks like quartz-monzonite and granite suites caused by a strong plagioclase fractionation (**Table 3**). The Th/U ratios show a decreasing trend from 0.6 to 0.8 of the volcanic/sub-volcanic rocks to values <0.4 of the post-ore granite, quartz-monzonite, and porphyries of the Buchim porphyry, as well (Lehmann et al., 2013).

The average Hf isotopic compositions of all magmatic rocks are plotted together with those from the Osogovo intrusion (Grozdev et al., 2017); the time-corrected data range from ε-Hf of 2.43 to −3.35. The older magmatic suite (**Figure 13**, Phase I) shows positive ε-Hf between 2.43 and 1.44, whereas granitic, quartz-monzonitic, and quartz-monzo-dioritic rocks have ε-Hf between −1.29 and −3.35, which demonstrates the

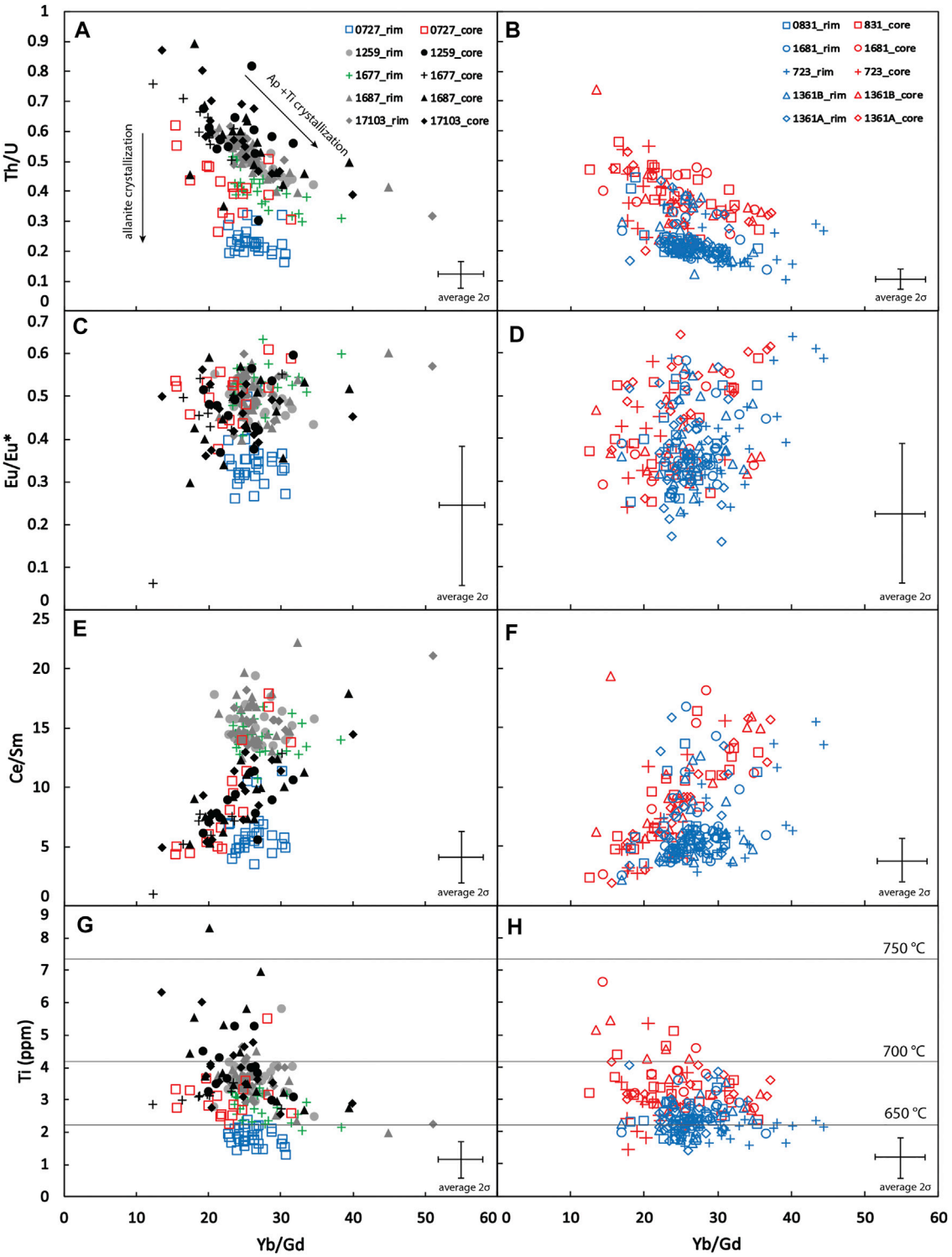

FIGURE 12 | Zircon trace element plots Th/U, Ce/Sm, Ti vs. Yb/Gd of the rhyodacite, granite (17,103, 1,687), granite/rhyodacite (1,259), granite (1,677), granite (CP, 0,723), granite (CP, 0,727), quartz–monzonite, (CP, 1361A), granite (PP, 0,831), quartz–monzonite (1361B), and quartz-monzo-diorite (PP, 1,681) samples. Black and red symbols refer to zircon core LA–ICP–MS measurements, and gray, green, and blue symbols display the rim values. Abbreviation: G = granite, G/R = granite/rhyodacite, QMD = quartz-monzo-diorite, and QM = quartz–monzonite.

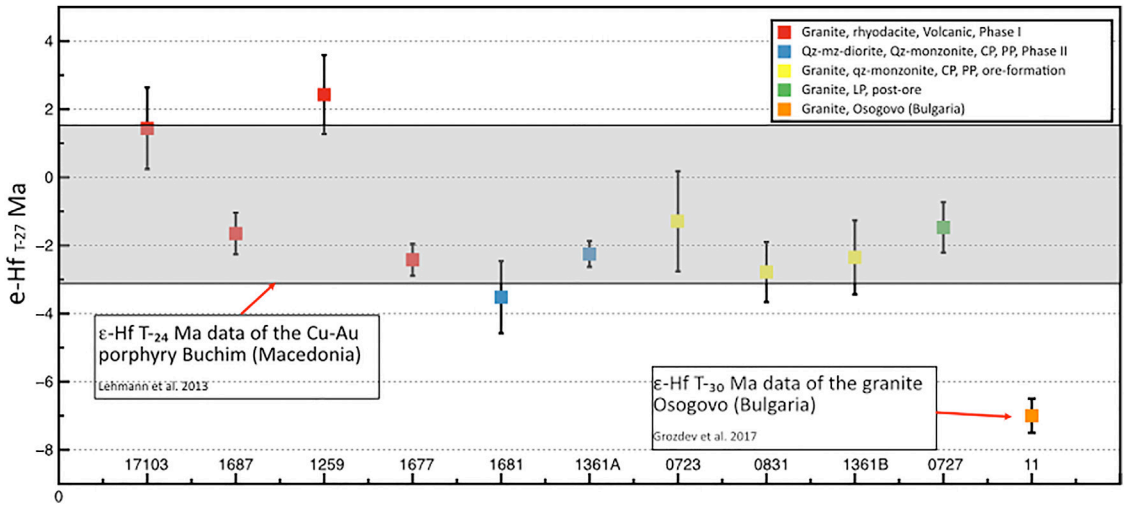

FIGURE 13 | ε-Hf data of KMC, Cu-Au porphyry (Lehmann et al., 2013) Buchim (North Macedonia), and the 29.5 Ma-old intrusion of Osogovo (Grozdev et al., 2017).

descending trend from older to younger magmatic rocks (**Figure 13**; **Supplementary Table S8**). The data of sub-/volcanic rocks are positive in ε-Hf; all intrusive rocks are similar in the ε-Hf range, and the older intrusion (29.5 Ma) of Osogovo (Grozdev et al., 2017) has a stronger crustal input with an ε-Hf values at −7.

DISCUSSION

Different Timescales of Processes Related to Magmatic Evolution of the KMC, the Mineralization, and Skarnitization Events

The CA–ID–TIMS data of the older magmatic group (**Figure 10**), the granitic porphyry (EOKSC 1677; age of 28.964 ± 0.01 Ma), and the granite (EOKSC 17103; age of 29.343 ± 0.03 Ma) yield $^{206}Pb/^{238}U$ ages that do not overlap within error uncertainties with the data of the porphyries of the syn- and post-ore formation (**Figure 10**). The next magmatic event (Phase II, **Figure 10**) starts with the CP quartz-monzonitic porphyry intrusion (EOKSC 1361A) with an emplacement age of 27.733 ± 0.03 Ma; the individual magmatic lifetime of this porphyry (EOKSC 1361A) with a range of 414 ± 45 ka is similar to that of Phase I (**Figure 10**). The time gap (1.231 Ma, **Figure 10**) between the quartz-monzonite EOKSC 1361A (Phase II) and the older magmatic group (Phase I, **Figure 10**) is remarkable and probably points to two independent geological events. The intrusion age of the quartz-monzonite porphyry (EOKSC 1361A, CP) defines the start of the mineralization at the KMC (**Figure 10**, **15**). The quartz-monzonitic porphyries (EOKSC 1361B, and 0,831, PP) crosscut the porphyry EOKSC 1361A and mark the end of the mineralization event at 27.607 ± 0.02 Ma (**Figure 10**). The difference in age (112 ± 45 ka) between both, the youngest zircon grains of the EOKSC 1361A and the EOKSC 0831 rock, defines the lifetime of the ore formation process. The last and the youngest magmatic phase of the granitic rock EOKSC 0727 (LP) shows an emplacement age of 27.583 ± 0.031 Ma, which overlaps within the uncertainty with two members of the ore formation phase (EKOSC 1361B and EKOSC 0831, **Figure 10**).

The obtained lifetime of the ore formation at the KMC with 112 ± 45 ka (**Figure 10**) is only a maximum duration because ore mineralization could be on much shorter timescales (Buret et al., 2016; Large et al., 2021). These numbers are consistent with models discussed by Weis et al. (2012) where timescales of porphyry ore formation within a porphyry stock are calculated between 50 and 100 Ka. To date, no clear relationship between the duration of magmatic–hydrothermal activity and the size of epithermal/hydrothermal deposits was identified from studies applying high-precision CA–ID–TIMS geochronology. Comparison of published datasets (Buret et al., 2016; Tapster et al., 2016; Large et al., 2018; Large et al., 2021) reveals maximum durations of metal-forming events of between tens of thousands of years and 10^5 yr. Although these studies are so far constrained to deposits of <10 Mt of contained Cu, these cover deposits that range over at least one order of magnitude in size (Koloula vs. Batu Hijau) (Tapster et al., 2016; Large et al., 2020). A correlation between the duration of the mineralizing event and the total mass of the deposited metal had been previously suggested based on compilations of different geochronological data sets (Lehmann et al., 2013; Chelle-Michou et al., 2017; Chiaradia, 2020). Longer durations of ore formation (> 1 Myr) were suggested based on Re–Os geochronology on molybdenite at the giant porphyry deposits and deposit clusters in Chile (> 50 Gt Cu; El Teniente), (Cannell et al., 2005 and Maksaev et al., 2004; Rio Blanco, Deckart et al., 2012) and Chuquicamata, (Barra et al., 2013). Mineralizing timescales of copper (and gold) were calculated by subtracting the youngest from the oldest Re–Os date. Thus, the large tonnage of these deposits could be the result of the

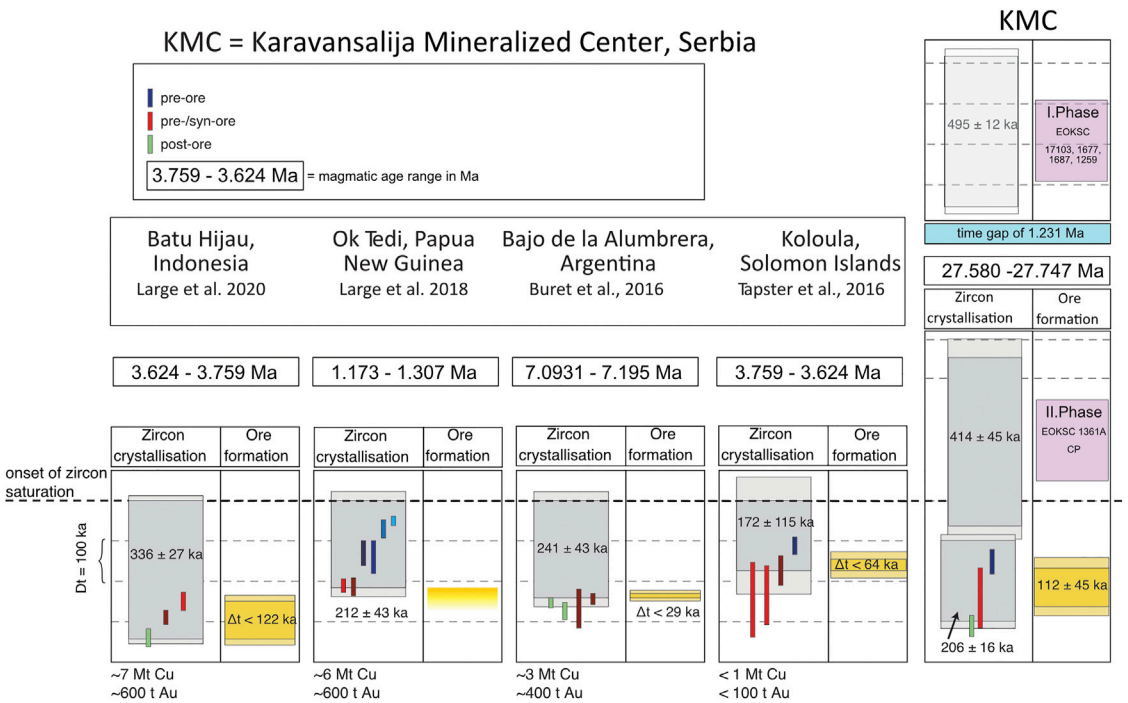

FIGURE 14 | Overview of high-precision geochronology studies on porphyry deposits. Data for Ok Tedi, Bajo de la Alumbrera, and Koloula are from Large et al. (2018), Buret et al. (2016), and Tapster et al. (2016), respectively. Colored vertical bars are emplacement ages of different intrusive rocks described from these deposits and categorized as pre-ore, pre-, and syn-ore, and post-ore intrusion. Deposit size decreases from left to right (tonnages from Cooke et al., 2005). Diagrams are aligned so that the onset of zircon crystallization overlaps in all deposits. Gray bars indicate the recorded duration of zircon crystallization. Yellow bars illustrate the maximum duration of total ore formation. The yellow bar fading out downward indicates the absence of a post-ore intrusion and the inability to constrain the total duration of ore formation.

superimposition of several ore-forming mid-to upper crustal magmatic systems. As the correlation of the deposit size and timescales of shallow magmatic–hydrothermal systems are currently ambiguous, we would argue that other variables could be the dominant factors controlling the deposit size, such as magma reservoir size, magma or fluid chemistry, fluid release, geological-tectonic situation and focusing mechanisms, or the metal precipitation efficiency. In that region (SW Serbia, North Macedonia), there are several magmatic occurrences with U–Pb ages between 23 and 35 Ma; the active Cu-porphyry mine at Buchim–Damjan–Borov Dol (North Macedonia) shows an Oligocene age of 24.5 Ma (Lehmann et al., 2013a), and the Cu-porphyry at Ilovitsa in SE (North Macedonia) has a magmatic Eocene/Oligocene age of 35 Ma.

Zircon crystallization over ~ 200 kyr before the onset of ore formation recorded at the KMC is consistent with other high-precision geochronological studies on ore deposits (**Figure 14**: Buret et al., 2016; Tapster et al., 2016; Large et al., 2018, Large et al., 2021). The lack of variation observed in these deposits suggests the necessity of a long-lived and continuously crystallizing magma reservoir preceding the formation of economically significant ore deposits. The recorded ~ 200 kyr of protracted zircon crystallization could indicate a period of volatile enrichment as a result of fractional crystallization and cooling of the magma reservoir before porphyry emplacement. The geochronological data from the KMC region are further evidence that magmatic emplacement (Phase I, **Figure 10**), reactivation of magma emplacement (Phase II), and ore formation (< 100 kyr) are the products of a longer-term evolution (a few 100 kyr, **Figures 10**, **14**) of a large magma reservoir underlying the ore deposit that is the main driver of ore formation (von Quadt et al., 2011; Chelle-Michou et al., 2014; Buret et al., 2016; 2017; Tapster et al., 2016; Large et al., 2018). Magma reservoirs capable of forming porphyries and epithermal deposits are in turn part of a longer-term (several Myr) evolution of lithosphere-scale magma systems (Sasso, 1998; Rohrlach et al., 2005; Longo et al., 2010; Rezeau et al., 2016), which is consistent with the 2 Myr record of intrusive rocks preceding porphyry emplacement and ore formation recorded in e.g., the Batu Hijau district (Garwin, 2000; Wawryk and Foden, 2017).

Reconstructing the Chemical and Physical Evolution of the Magma Reservoir

Th/U and Yb/Gd and Ce/Sm ratios and Ti concentrations of zircon grains are commonly used as proxies for the degree of crystal fractionation within a magma reservoir (Samperton et al., 2015; Large et al., 2021). The decreasing Th/U ratios and increasing Yb/Gd ratios between samples and from cores to rims are indicative of progressive melt differentiation during zircon crystallization.

Trace element populations of zircons from the two rhyodacitic/granitic rocks demonstrate that the crystallizing

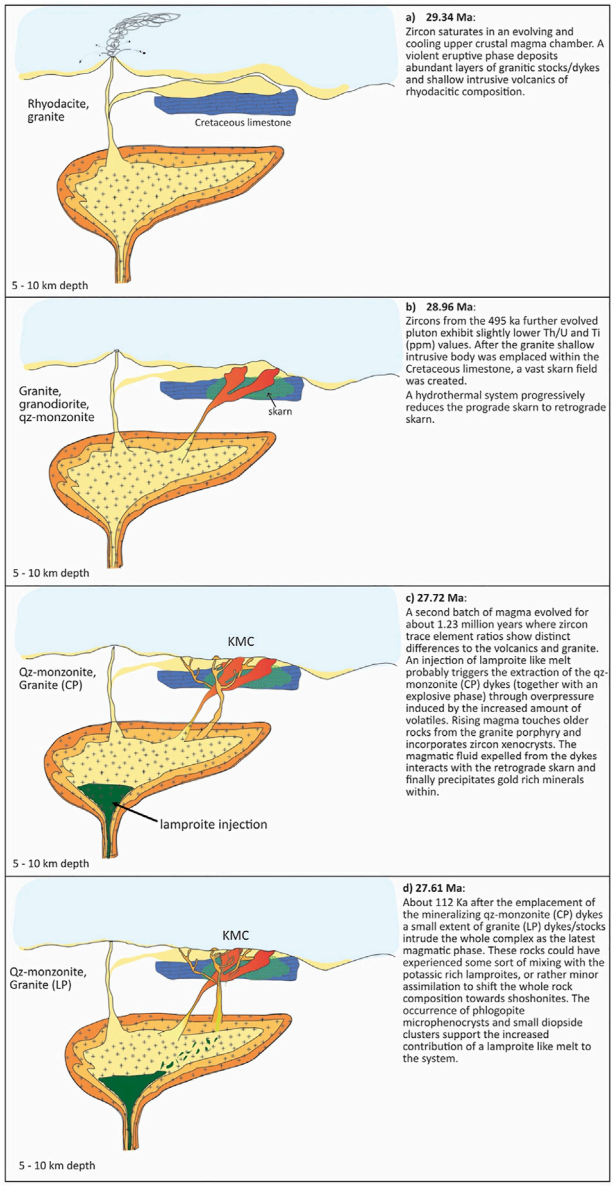

FIGURE 15 | Model for the formation of the KMC (not to scale).

magma at the time of emplacement of the older magmatics (EOKSC 1677, 1,687, and 17103) was hot and less evolved magma (**Figure 12G**) than at the time of emplacement of the younger quartz-monzonite dyke suite (i.e., 1.231 Myr after emplacement of the old porphyries, respectively). The good correlation of proxies indicating progressive differentiation (Th/U and Yb/Gd) with decreasing Ti concentrations (**Figures 12E,F**) indicates that the magma reservoir cooled during concurrent crystallization and melt evolution. *In situ* analyses of cores and rims are evidence of an evolving magma reservoir over the course of individual zircon crystallization (decreasing Ti; **Figures 12E,F**). Core–rim systematics of zircons from the old granite–rhyodacite further demonstrate cooling during protracted zircon growth (**Figure 12**). The coherent zircon trace element systematics recording melt differentiation over time are commonly inferred to result from zircon crystallization within a homogenous magma that evolved continuously (**Figures 12**, **14**). The numerical model (Karakas et al., 2017) describes a system made up of a magma chamber in the upper crust that is connected with further deeper chambers in the lower crust. In principle, the model might indicate that all zircons analyzed in this study have crystallized from the same reservoir, where the zircons from the granite and rhyodacite reflect the earliest crystallized zircons from the least evolved melt. Hot source magma forms in the mantle or lower crust before rising through cracks and chimneys into the upper magma chamber (upper crust). It forms a reservoir, which cools down and partially crystallizes but can survive as a crystal mush for hundreds of thousands of years (Karakas et al., 2017).

However, the > 1.231 Myr time gap (**Figure 10**) is longer than the thermal lifetime of any recognized upper-crustal magmatic body (200–400 ky) (Wotzlaw et al., 2013; Large et al., 2020). We, therefore, consider two possible models: either the zircons within the rhyodacite/granite porphyry represent a separate crustal magmatic system not directly related to the younger ore-forming quartz-monzonitic intrusion system or the latter resulted from the same chamber that evolved through magma replenishment (model shown on **Figure 15**). Our results also require that the majority of zircon crystallization occurred in zircon-saturated reservoirs at deeper crustal levels prior to final magma emplacement and cooling, which has implications for using zircon U–Pb geochronology to infer upper crustal magma residence times (Barboni et al., 2015).

Irregular zircon trace element systematics in other intrusive magmatic settings have been explained with crystallization in non-homogenized and small melt batches sometimes, with contemporaneous incremental magma in addition to the mushy magma reservoir (Schoene et al., 2012; Tapster et al., 2016; Buret et al., 2016). Geochemically, similar zircon chemistries of granite, quartz-monzodiorite, or quartz–monzonites could also result from chemical stability as the magma reservoir reached the "petrological trap" at a crystallinity of ~ 55–65% (Caricchi and Blundy, 2015), where the crystal fraction does not change over a broad temperature interval. Rim analyses that plot more outside the mineral co-crystallization trends than the respective core analyses (**Figures 12B,C**) could suggest latest crystallization within a nearly solidified magma that can be characterized by unsystematically variable trace element signatures (Buret et al., 2016; Lee et al., 2021). Alternatively, they could indicate thermal and possibly chemical rejuvenation of the magma. The latter would help for explaining the recorded thermal stability over tens of thousands of years. It is not possible to unambiguously identify one of the two mechanisms as dominant, and a concurrence of both is feasible. We, therefore, propose that in-between the emplacement of the old and young granite–quartz–monzonite, the underlying magma reservoir was in a thermally and chemically stable and crystal-rich state and was most likely affected by incremental magma underplating. This suggests that Au deposits form after a few hundred thousand years of cooling and crystallization, potentially within an originally melt-rich magma reservoir.

The ratios of Eu/Eu* and Ce/Sm in zircon are suggested in various studies (Ballard et al., 2002; Chelle-Michou et al., 2014) to record the oxidation state of the magma. Ce^{4+} is much more compatible in zircon than Ce^{3+}, which is why zircon commonly presents a positive Ce anomaly (Hoskin and Schaltegger, 2003). The Cu–(Au) systems are often associated with oxidized magmas (Richards, 2011), which document the high Ce anomaly accompanied by decreasing Ti concentrations in case of the most evolved magmas. Additionally, due to the the higher uptake of MREEs than LREEs, in some minerals, the residual melt will enrich in Ce relative to Sm. However, an opposite trend at the KMC of decreasing Ce/Sm with decreasing age is recognized over all samples. The same trend is best visualized in the Th/U vs. Ce/Yb plot, where the rim values decrease from the volcanics to older sub-volcanics and finally to the quartz-monzonitic/granitic dykes. This strong depletion of Ce in combination of Th is most probably due to allanite fractionation (**Figure 12**). The observed weak Eu anomaly is more consistent due to commonly strong plagioclase fractionation, which nevertheless, is reduced to some extent by coeval titanite/apatite crystallization (Deering and Bachmann, 2010). The Hf isotopes support the presence of a cooling magma chamber with increased crustal assimilation with time because the ε-Hf values evolve from more "primitive" +3.5 ± 1.3 for the older volcanics and granite stocks/dykes to −0.8 ± 0.9 for the younger more evolved quartz-monzonitic-granitic rocks (**Figure 13**); the Late Oligocene porphyries at the Cu–Au Buchim deposit (North Macedonia) or Oligocene rocks in the Osogovo base metal region (Bulgaria) show similar evolution with crustal-dominated source material (**Figure 13**).

Model for the Formation of the Karavansalija Mineralized Center

The geochronological and geochemical data set lead to a geodynamic model (**Figure 14**) which is proposed for the evolution of the magmatic–hydrothermal system and formation of the Au ± Cu–Pb–Zn mineralization of the Karavansalija Mineralized Center.

1) In a first stage at ~29.3 Ma, zircon saturates in a composite upper crustal magma chamber (5–10 km depth) of calc-alkaline character probably generated by melting of mafic lower crustal material or subduction-modified subcontinental mantle lithosphere. The upper-crustal chamber will be recharged from a deeper level reservoir (Barboni et al., 2015). The magma consists of a mixture of liquid and crystal mush, fractionating during cooling, generating trends of titanite ± apatite ± amphibole crystallization recorded in a zircon trace element pattern (Szymanowski et al., 2017). Rejuvenation of hot and water-saturated magma into the chamber could lead to over pressuring of the cooling mush in the apex through further exsolution of volatiles, finally giving rise to an explosive event with the deposition of andesite-rhyodacitic pyroclastic rocks, lava flows, and shallow intrusives. Hence, this leads to the formation of the widespread dacitic volcanic rocks observed in the Rogozna volcanic suite.
2) Further evolution and cooling of the magma chamber of about 495 Ka causing increased titanite, apatite ± allanite crystallization shifted the Th/U and Ti (ppm) to slightly lower values. Through another injection or tectonic trigger, the granitic porphyry is emplaced (~29 Ma) into the Cretaceous flysch sediments and overlying volcanics. These shallow intrusive bodies generated a vast skarn field within the Copper Canyon and Shanac region, producing prograde exoskarns and endoskarns.
3) In the meantime, a new batch of the upper crustal magma chamber evolves for a further 1.2 million years, showing trends of increased crustal assimilation in the Hf isotopic composition recorded in those zircons. The assimilation of crustal rocks containing allanite may have enriched the magma in LREE and Th (Szymanowski et al., 2017). The magma batch progressively cools and fractionates allanite together with titanite, amphibole, and zircon. However, allanite overprints the trace element variations seen within zircon from other crystallizing minerals, decreasing very efficiently the Th/U, Ce/Sm, and Ce/Yb ratios. An injection of a lamproite melt with abundant volatiles into the base of the andesitic crystal mush likely initiates the extraction of the crowded porphyries at 27.759 ± 0.013 Ma with shallow intrusive dykes and stocks analyzed in this study. These dykes cut the older granitic porphyry and the associated skarn field, strongly interacting with them. The accompanied magmatic fluids enriched in metals and volatiles built up a hydrothermal system. Retrograde hydrothermal alteration of the skarn field and subsequent precipitation of Au-rich minerals, e.g., arseno-pyrite, base-metal sulfides, and native Au close to sulfides, form mineralization in the KMC district.
4) After the emplacement of the quartz-monzonitic dykes, the residual magma could have partially mixed with the lamproite melt or more likely assimilated some of the lamproites, shifting the whole-rock composition toward shoshonites, which is recognized in the whole-rock chemistry plots (**Figures 7**, **8**). Then, a smaller batch of granitic dykes are emplaced in another pulse 119 Ka after the quartz-monzonitic dykes at 27.607 ± 0.02 Ma cutting them and the mineralized skarn. In these rocks, abundant phlogopite micro-phenocrysts, phlogopitization of biotite, small diopside clusters, and diopside reaction-rims on quartz indicate increased temperatures and disequilibrium conditions, which support the incorporation of a potassium-rich melt before extraction.

CONCLUSION

The Pb–Zn–Ag–Au mineralization of the KMC at Rogozna Mt. in southwestern Serbia is linked to a shallow intrusive porphyritic intrusion, which is typical for the abundant metal ore deposits and minor precious metal deposits in the SMM-MB of the Oligocene age. The geochemical evolution of the ore-forming magma chamber could be tracked by analyzing zircon from initial zircon saturation through the emplacement of the various porphyries. *In situ* LA–ICP–MS and high-precision

CA–ID–TIMS analyses lead to the discovery of the presence of two evolved magmas with distinct trace element patterns. A first stage of violent eruptive and shallow intrusive volcanic activity of granitic/rhyodacitic composition at ca. 29.34 Ma is followed by the intrusion of another porphyritic body at ca. 28.96 Ma trending toward shoshonitic composition into Cretaceous limestone, producing a skarn reaction zone. A separate magma chamber evolved with increased crustal assimilation recorded by the Hf isotopes and with a strong allanite fractionation trend seen on zircon trace element ratios. The input of a new melt into the base of the magma chamber increased the fluid pressure and likely provided additional fluids, metals, and sulfur before the emplacement of the quartz-monzonitic dykes into the skarn zone, precipitating the gold in a retrograde hydrothermal system starting at ca. 27.76 Ma. About 112 ka later (27.62 Ma), the last pulse of the quartz-monzonitic-porphyritic magma cuts the mineralization and records the maximum duration of mineralization at the KMC. These melts show signs of increased temperature and disequilibrium through the injection of a potassium-rich melt recorded from the abundant phlogopite micro-phenocrysts, small diopside clusters, and diopside reaction-rims on quartz recognized under the microscope. Nearby occurrences of significant base-metal mineralization, e.g., Crnac, Rudnik, or Veliki Majdan, are all thought to be associated with trachy-andesitic (quartz latitic) porphyry dykes but are not very precisely dated. The quartz-monzonitic dykes responsible for the mineralization at the KMC display many similarities with the described porphyries at Crnac (e.g., crowded phenocrysts, shoshonitic character, disequilibrium textures, and trace element pattern), and they likely share the same magmatic source responsible for their mineralization.

The geochronological data set shows that without CA–ID–TIMS dating the individual magmatic pulse responsible for the mineralization could not be identified; however, the LA–ICP–MS data help to see variation within a single zircon population and could reveal trends between core and rim measurements. Additionally, the laser technique records the homogeneity of the ablated material and therefore helps to interpret the ID–TIMS data where for example the input of xenocrystic or inherited cores cannot be determined. So far not many Cenozoic ore deposits in the Balkan area have been dated with the CA–TIMS U/Pb dating methods. This study has proven the benefits of a high-precision dating resolution in resolving different magmatic pulses within a single magmatic system. Consequently, the mineralization, which is typically associated with a magmatic intrusive event, can be traced and timed more precisely. Further work in the Balkan region involving U/Pb TIMS dating will help to delineate the various mineralizations with respect to their time of formation, link to magmatism, and the tectonic frame in which they were built.

DATA AVAILABILITY STATEMENT

The original contributions presented in the study are included in the article/**Supplementary Material**, further inquiries can be directed to the corresponding author.

AUTHOR CONTRIBUTIONS

JH, AQ, RB, IP, VC, and TB have contributed to the study; IP was responsible for the CA–TIMS analytical part and data set; JH has produced the Laser ICP–MS data set.

FUNDING

The research was funded by the Swiss National Foundation grant (SNF) number IZ74Z0_16512 ("Strategic PArtnership for Critical Improvements in Methodology of studying and teaching of mineral resources—SPACIM") and Grant Number 200021_146651 (Mineral resources: Physical dynamics driving chemical enrichment of rare metals).

ACKNOWLEDGMENTS

The project became possible during the exploration activities of Euromax Resources Ltd. held by Eldorado Gold that provided access to boreholes and samples with clear temporal and spatial relationships of the intrusions, skarns, and the Pb–Zn–Bi–Ag–Au mineralization. JH thanks Simon Large for motivation during analytical work and discussions on earlier versions of the study results.

SUPPLEMENTARY MATERIAL

The Supplementary Material for this article can be found online at: https://www.frontiersin.org/articles/10.3389/feart.2021.798701/full#supplementary-material

REFERENCES

Andrić, N., Vogt, K., Matenco, L., Cvetković, V., Cloetingh, S., and Gerya, T. (2018). Variability of Orogenic Magmatism during Mediterranean-Style continental Collisions: A Numerical Modelling Approach. *Gondwana Res.* 56, 119–134.

Bachmann, O., Charlier, B. L. A., and Lowenstern, J. B. (2007). Zircon Crystallization and Recycling in the Magma Chamber of the Rhyolitic Kos Plateau Tuff (Aegean Arc). *Geol.* 35, 73–76. doi:10.1130/g23151a.1

Baker, T. (2019). Gold ± Copper Endowment and Deposit Diversity in the Western Tethyan Magmatic Belt, Southeast Europe: Implications for Exploration. *Econ. Geol.* 114, 1237–1250. doi:10.5382/econgeo.4643

Ballard, J. R., Palin, M. J., and Campbell, I. H. (2002). Relative Oxidation States of Magmas Inferred from Ce(IV)/Ce(III) in Zircon: Application to Porphyry Copper Deposits of Northern Chile. *Contrib. Mineral. Petrol.* 144, 347–364. doi:10.1007/s00410-002-0402-5

Banik, T. J., Coble, M. A., and Miller, C. F. (2017). Porphyry Cu Formation in the Middle Jurassic Yerington Batholith, Nevada, USA: Constraints from Laser

Raman, Trace Element, U-Pb Age, and Oxygen Isotope Analyses of Zircon. *Geosphere* 13, 1113–1132. doi:10.1130/ges01351.1

Banješević, M., Cvetković, V., von Quadt, A., Obradović, D. L., Vasić, N., Pačevski, A., et al. (2019). New Constraints on the Main Mineralization Event Inferred from the Latest Discoveries in the Bor Metallogenetic Zone (BMZ, East Serbia). *Minerals* 9, 672. doi:10.3390/min9110672

Barboni, M., Schoene, B., Ovtcharova, M., Bussy, F., Schaltegger, U., and Gerdes, A. (2013). Timing of Incremental Pluton Construction and Magmatic Activity in a Back-Arc Setting Revealed by ID-TIMS U/Pb and Hf Isotopes on Complex Zircon Grains. *Chem. Geology.* 342, 76–93. doi:10.1016/j.chemgeo.2012.12.011

Barboni, M., Annen, C., and Schoene, B. (2015). Evaluating the Construction and Evolution of Upper Crustal Magma Reservoirs with Coupled U/Pb Zircon Geochronology and thermal Modeling: A Case Study from the Mt. Capanne Pluton (Elba, Italy). *Earth Planet. Sci. Lett.* 432, 436–448. doi:10.1016/j.epsl.2015.09.043

Borojević Šoštarić, S., Cvetković, V., Neubauer, F., Palinkaš, L. A., Bernroider, M., and Genser, J. (2012). Oligocene Shoshonitic Rocks of the Rogozna Mts. (Central Balkan Peninsula): Evidence of Petrogenetic Links to the Formation of Pb–Zn–Ag Ore Deposits. *Lithos* 148, 176–195.

Barra, F., Alcota, H., Rivera, S., Valencia, V., Munizaga, F., and Maksaev, V. (2013). Timing and Formation of Porphyry Cu–Mo Mineralization in the Chuquicamata District, Northern Chile: New Constraints from the Toki Cluster. *Miner. Deposita* 48, 629–651. doi:10.1007/s00126-012-0452-1

Bowring, J. F., McLean, N. M., and Bowring, S. A. (2011). Engineering Cyber Infrastructure for U-Pb Geochronology: Tripoli and U-Pb_Redux. *Geochem. Geophys. Geosystems* 12. doi:10.1029/2010gc003479

Budinov, Z. D., Yonezu, K., Tindell, T., Gabo-Ratio, J. A., Milutinovic, S., Boyce, A. J., et al. (2015). Copper–Gold Skarn Mineralization at the Karavansalija Ore Zone, Rogozna Mountain, Southwestern Serbia. *Resour. Geol.* 65, 328–344.

Buret, Y., von Quadt, A., Heinrich, C., Selby, D., Wälle, M., and Peytcheva, I. (2016). From a long-lived upper-crustal magma chamber to rapid porphyry copper emplacement: Reading the geochemistry of zircon crystals at Bajo de la Alumbrera (NW Argentina). *Earth Planet. Sci. Lett.* 450, 120–131. doi:10.1016/j.epsl.2016.06.017

Burt, D. M. (1989). Compositional and phase relations among rare earth element minerals. *Rev. Miner.* 21, 259–307.

Burkhard, R. (2017). *Style, Relative Timing and Precipitation Conditions of the Au Mineralisation at Karavansalija Ore Zone, Rogozna Mts*. ETH Zurich, 54. SerbiaMaster.

Cannell, J., Cooke, D. R., Walshe, J. L., and Stein, H. (2005). Geology, mineralization, alteration, and structural evolution of the El Teniente porphyry Cu-Mo deposit. *Econ. Geol.* 100, 979–1003.

Caricchi, L., and Blundy, J. (2015). The Temporal Evolution of Chemical and Physical Properties of Magmatic Systems. *Geol. Soc. Lond. Spec. Publ.* 422, 1–15. doi:10.1144/sp422.11

Chelle-Michou, C., Chiaradia, M., Ovtcharova, M., Ulianov, A., and Wotzlaw, J.-F. (2014). Zircon Petrochronology Reveals the Temporal Link between Porphyry Systems and the Magmatic Evolution of Their Hidden Plutonic Roots (The Eocene Coroccohuayco deposit, Peru). *Lithos* 198-199, 129–140. doi:10.1016/j.lithos.2014.03.017

Ćebić, V. (1990). *Konačni Izveštaj o geološko-petrološkom i Geohemijskom Izučavanju Tercijarnog Magmatskog Kompleksa Surduličke Oblasti*. Fond Geoinstituta: Beograd.

Chelle-Michou, C., Rottier, B., Caricchi, L., and Simpson, G. (2017). Tempo of Magma Degassing and the Genesis of Porphyry Copper Deposits. *Sci. Rep.* 7, 40566. doi:10.1038/srep40566

Chiaradia, M., Schaltegger, U., Spikings, R., Wotzlaw, J.-F., and Ovtcharova, M. (2013). How Accurately Can We Date the Duration of Magmatic-Hydrothermal Events in Porphyry Systems?--An Invited Paper. *Econ. Geology.* 108, 565–584. doi:10.2113/econgeo.108.4.565

Chiaradia, M., Schaltegger, U., and Spikings, R. (2014). *Time Scales of Mineral Systems—Advances in Understanding over the Past Decade*.

Chiaradia, M. (2020). *Stochastic Modelling of Deep Magmatic Controls on Porphyry Copper deposit Endowment: Scientific Reports*, 11.

Condon, D. J., Schoene, B., McLean, N. M., Bowring, S. A., and Parrish, R. R. (2015). Metrology and Traceability of U-Pb Isotope Dilution Geochronology (EARTHTIME Tracer Calibration Part I). *Geochim. Cosmochim. Acta* 164, 464–480. doi:10.1016/j.gca.2015.05.026

Cvetkovic, A., Ivanovic, M., and Saric, K. (2006). The Role of Streptococcus Mutans Group and Salivary Immunoglobulins in Etiology of Early Childhood Caries. *Serbian Dent J.* 53, 113–123. doi:10.2298/sgs0602113c

Cvetković, V., Poli, G., Christofides, G., Koroneos, A., Pecskay, Z., Resimić-Sarić, K., et al. (2007). The Miocene granitoid rocks of Mt. Bukulja (central Serbia): evidence for pannonian extension-related granitoid magmatism in the northern Dinarides. *Eur. J. Mineral.* 19, 513–532.

Cvetković, V., Pecskay, Z., and Saric, K. (2016). Cenozoic igneous tectonomagmatic events in the Serbian part of the Balkan Peninsula: Inferences from K/Ar geochronology. *Acta Vulcanologica* 25, 113–125.

Davidson, J., Turner, S., Handley, H., Macpherson, C., and Dosseto, A. (2007). Amphibole "sponge" in arc crust?. *Geology* 35, 787–790.

Deckart, K., Clark, A. H., Cuadra, P., and Fanning, M. (2012). Refinement of the time-space evolution of the giant Mio-Pliocene Rio Blanco-Los Bronces porphyry Cu–Mo cluster, Central Chile: new U–Pb (SHRIMP II) and Re–Os geochronology and 40Ar/39Ar thermochronology data. *Miner. Deposita* 48, 57–79. doi:10.1007/s00126-012-0412-9

Deering, C. D., and Bachmann, O. (2010). Trace Element Indicators of crystal Accumulation in Silicic Igneous Rocks. *Earth Planet. Sci. Lett.* 297, 324–331. doi:10.1016/j.epsl.2010.06.034

Defant, M. J., and Drummond, M. S. (1993). *Mount St. Helens: Potential Example of the Partial Melting of the Subducted Lithosphere in a Volcanic Arc: Geology* 21, 547–550.

Erak, D., Matenco, L., Toljić, M., Stojadinović, U., Andriessen, P. A. M., Willingshofer, E., et al. (2017). From Nappe Stacking to Extensional Detachments at the Contact between the Carpathians and Dinarides - the Jastrebac Mountains of Central Serbia. *Tectonophysics* 710-711, 162–183. doi:10.1016/j.tecto.2016.12.022

Ferry, J. M., and Watson, E. B. (2007). New Thermodynamic Models and Revised Calibrations for the Ti-In-Zircon and Zr-In-Rutile Thermometers. *Contrib. Mineral. Petrol.* 154, 429–437. doi:10.1007/s00410-007-0201-0

Frei, R. (1992). Isotope (Pb, Rb-Sr, S, O, C, U-Pb) geochemical investigations on Tertiary 830 intrusives and related mineralizations in the Serbomacedonian Pb-Zn, Sb+ Cu-Mo metallogenetic province in northern Greece. PhD thesis, ETH Zurich.

Gallhofer, D., Quadt, A. V., Peytcheva, I., Schmid, S. M., and Heinrich, C. A. (2015). Tectonic, Magmatic, and Metallogenic Evolution of the Late Cretaceous Arc in the Carpathian-Balkan Orogen. *Tectonics* 34, 1813–1836. doi:10.1002/2015tc003834

Garwin, S. L. (2000). *The Setting, Geometry and Timing of Intrusionrelated Hydrothermal System in the Vicinity of the Batu Hijau Porphyry Copper-Gold deposit*. Sumbawa, Indonesia: University of Western Australia.

Gehrels, G. E., Valencia, V. A., and Ruiz, J. (2008). Enhanced Precision, Accuracy, Efficiency, and Spatial Resolution of U-Pb Ages by Laser Ablation-Multicollector-Inductively Coupled Plasma-Mass Spectrometry. *Geochem. Geophys. Geosyst.* 9. doi:10.1029/2007gc001805

Gelder, I. E., Matenco, L., Willingshofer, E., Tomljenović, B., Andriessen, P. a. M., Ducea, M. N., et al. (2015). The Tectonic Evolution of a Critical Segment of the Dinarides-Alps Connection: Kinematic and Geochronological Inferences from the Medvednica Mountains, NE Croatia. *Tectonics* 34, 1952–1978. doi:10.1002/2015tc003937

Georgiev, S., von Quadt, A., Heinrich, C. A., Peytcheva, I., and Marchev, P. (2012). *Time evolution of a rifted continental arc: Integrated ID-TIMS and LA-ICPMS study of magmatic zircons from the Eastern Srednogorie, Bulgaria: Lithos*. Bulgaria: Lithos 53, 57–67.

Grozdev, V., Peytcheva, I., von Quadt, A., Vassileva, R., and Georgiev, S. (2017). Analysis of the Zircon Population and Sr-Isotope Data of the Paleogene Igneous Rocks from Kyustendil Area, SW Bulgaria. *Geol. Balc.* 46, 143–151.

Halter, W. E., Bain, N., Becker, K., Heinrich, C. A., Landtwing, M., VonQuadt, A., et al. (2004). From Andesitic Volcanism to the Formation of a Porphyry Cu-Au Mineralizing Magma Chamber: the Farallón Negro Volcanic Complex, Northwestern Argentina. *J. Volcanol. Geotherm. Res.* 136, 1–30. doi:10.1016/j.jvolgeores.2004.03.007

Hörler, J. (2017). The Karavansalija Ore Zone at Rogozna Mt. In Southwestern Serbia: Magma Evolution and Time Relationship of Intrusive Events, Skarn Mineralization and Overlying Volcanics:

Hoskin, P. W. O., and Schaltegger, U. (2003). 2. The Composition of Zircon and Igneous and Metamorphic Petrogenesis. *Rev. Mineral. Geochem.* 53, 27–62. doi:10.1515/9781501509322-005

Janković, S. (1997). The Carpatho-Balkanides and Adjacent Area: a Sector of the Tethyan Eurasian Metallogenic belt. *Miner. Deposita* 32, 426–433.

Jelenković, R., Milovanović, D., Koželj, D., and Banješević, M. (2016). The Mineral Resources of the Bor Metallogenic Zone: A Review. *Geol. Croat.* 69, 143–155. doi:10.4154/gc.2016.11

Kandic, M., Micic, I., Miletic, G., Markovic, D., and Milutinovic, S. (1987). *Metallogenic Characteristics of the Rogozna Field*. Geozavod-IMS, 1–126.

Karakas, O., Degruyter, W., Bachmann, O., and Dufek, J. (2017). Lifetime and Size of Shallow Magma Bodies Controlled by Crustal-Scale Magmatism. *Nat. Geosci.* 10, 446–450. doi:10.1038/ngeo2959

Keller, C. B., Schoene, B., and Samperton, K. M. (2018). A Stochastic Sampling Approach to Zircon Eruption Age Interpretation. *Geochem. Persp. Let.*, 31–35. doi:10.7185/geochemlet.1826

Klimm, K., Blundy, J. D., and Green, T. H. (2008). Trace Element Partitioning and Accessory Phase Saturation during H2O-Saturated Melting of Basalt with Implications for Subduction Zone Chemical Fluxes. *J. Petrol.* 49, 523–553. doi:10.1093/petrology/egn001

Koroneos, A., Poli, G., Cvetković, V., Krstić, D., and PECskay, Z. (2010). Petrogenetic and tectonic inferences from the study of the Mt Cer pluton (West Serbia). *Geol. Mag.* 148, 89–111.

Large, S. J. E., Quadt, A. v., Wotzlaw, J.-F., Guillong, M., and Heinrich, C. A. (2018). Magma Evolution Leading to Porphyry Au-Cu Mineralization at the Ok Tedi Deposit, Papua New Guinea: Trace Element Geochemistry and High-Precision Geochronology of Igneous Zircon. *Econ. Geology.* 113, 39–61. doi:10.5382/econgeo.2018.4543

Large, S. J. E., Wotzlaw, J. F., Guillong, M., Quadt, A. v., and Heinrich, C. A. (2020). *Resolving the Timescales of Magmatic and Hydrothermal Processes Associated with Porphyry deposit Formation Using Zircon U-Pb Petrochronology: Geochronology Discussions*, 1–39.

Large, S. J. E., Buret, Y., Wotzlaw, J. F., Karakas, O., Guillong, M., von Quadt, A., et al. (2021). Copper-mineralised Porphyries Sample the Evolution of a Large-Volume Silicic Magma Reservoir from Rapid Assembly to Solidification. *Earth Planet. Sci. Lett.* 563, 116877. doi:10.1016/j.epsl.2021.116877

Le Maitre, R. W. B., Dudek, P., Keller, A., Lameyre, J., Le Bas, J., Sabine, M. J., et al. (1989). *A Classification of Igneous Rocks and Glossary of Terms: Recommendations of the International Union of Geological Sciences, Subcommission on the Systematics of Igneous Rocks*. International Union of Geological Sciences.

Lee, R. G., Dilles, J. H., Tosdal, R. M., Wooden, J. L., and Mazdab, F. K. (2017). Magmatic Evolution of Granodiorite Intrusions at the El Salvador Porphyry Copper Deposit, Chile, Based on Trace Element Composition and U/Pb Age of Zircons. *Econ. Geology.* 112, 245–273. doi:10.2113/econgeo.112.2.245

Lee, R. G., Byrne, K., D'Angelo, M., Hart, C. J. R., Hollings, P., Gleeson, S. A., et al. (2021). Using Zircon Trace Element Composition to Assess Porphyry Copper Potential of the Guichon Creek Batholith and Highland Valley Copper deposit, South-central British Columbia. *Miner Deposita* 56, 215–238. doi:10.1007/s00126-020-00961-1

Lehmann, S., Barcikowski, J., von Quadt, A., Gallhofer, D., Peytcheva, I., Heinrich, C. A., et al. (2013). Geochronology, Geochemistry and Isotope Tracing of the Oligocene Magmatism of the Buchim-Damjan-Borov Dol Ore District: Implications for Timing, Duration and Source of the Magmatism. *Lithos* 180-181, 216–233. doi:10.1016/j.lithos.2013.09.002

Lesić, V., Márton, E., Gajić, V., Jovanović, D., and Cvetkov, V. (2019). Clockwise Vertical-axis Rotation in the West Vardar Zone of Serbia: Tectonic Implications. *Swiss J. Geosci.* 112, 199–215. doi:10.1007/s00015-018-0321-8

Lilov, P., Yanev, Y., and Marchev, P. (1987). K/Ar dating of the Eastern Rhodopes Paleogene magmatism. *Geologica Balcanica* 17, 49–58.

Longo, A. A., Dilles, J. H., Grunder, A. L., and Duncan, R. (2010). Evolution of calc-alkaline volcanism and associated hydrothermal gold deposits at Yanacocha, Peru. *Econ. Geol.* 105, 1191–1241.

Maksaev, V., Munizaga, F., and McWilliams, M. (2004). New Chronology for El Teniente, Chilean 916 Andes, from U-Pb, $^{40}Ar/^{39}Ar$, Re-Os, and Fission-Track Dating: Implications for the Evolution of a Supergiant Porphyry Cu-Mo Deposit', in Sillitoe, R.H., Perello, J. and Vidal, C.E. (ed.). *Andean Metallogeny: New Discoveries, Concepts, and Updates*. Littleton, CO: Society of Economic Geologists, 15–54.

Marchev, P., Raicheva , R., Downes, H., Vaselli, O., Chiaradia, M., and Moritz, R. (2015). Tectonic, Magmatic, and Metallogenic Evolution of the Late Cretaceous Arc in the Carpathian-Balkan Orogen. *Tectonics* 34, 1813–1836. doi:10.1002/2015tc003834

Maksaev, V., Munizaga, F., Fanning, M., Palacios, C., and Tapia, J. (2006). SHRIMP U-Pb Dating of the Antucoya Porphyry Copper deposit: New Evidence for an Early Cretaceous Porphyry-Related Metallogenic Epoch in the Coastal Cordillera of Northern Chile. *Miner Deposita* 41, 637–644. doi:10.1007/s00126-006-0091-5

Marchev, P., Kaiser-Rohrmeier, M., Heinrich, C., Ovtcharova, M., von Quadt, A., and Raicheva, R. (2005). 2: Hydrothermal Ore Deposits Related to post-orogenic Extensional Magmatism and Core Complex Formation: The Rhodope Massif of Bulgaria and Greece. *Ore Geol. Rev.* 27, 53–89. doi:10.1016/j.oregeorev.2005.07.027

Marchev, P., Georgiev, S., Raicheva, R., Peytcheva, I., von Quadt, A., Ovtcharova, M., et al. (2013). Adakitic magmatism in post-collisional setting: An example from the Early-Middle Eocene Magmatic Belt in Southern Bulgaria and Northern Greece. *Lithos* 180, 159–180.

Marchev, P., and Singer, B. (2002). *40Ar/39Ar Geochronology of Magmatism and Hydrothermal Activity of the Madjarovo Base-Precious Metal Ore District*. Eastern Rhodopes, Bulgaria: Geological Society, London, Special Publications, 204, 137–150.

Marchev, P., Kibarov, P., Spikings, R. A., Ovtcharova, M., Marton, I., and Moritz, R. (2010). *40Ar/39Ar and U-Pb Geochronology of the Iran Tepe Volcanic Complex*. Eastern Rhodopes: Geologica Balcanica, 39, 3–12.

Matenco, L., and Radivojević, D. (2012). On the Formation and Evolution of the Pannonian Basin: Constraints Derived from the Structure of the junction Area between the Carpathians and Dinarides. *Tectonics* 31. doi:10.1029/2012tc003206

Mattinson, J. M. (2005). Zircon U-Pb Chemical Abrasion ("CA-TIMS") Method: Combined Annealing and Multi-step Partial Dissolution Analysis for Improved Precision and Accuracy of Zircon Ages. *Chem. Geol.* 220, 47–66. doi:10.1016/j.chemgeo.2005.03.011

McLean, N. M., Bowring, J. F., and Bowring, S. A. (2011). An Algorithm for U-Pb Isotope Dilution Data Reduction and Uncertainty Propagation. *Geochem. Geophys. Geosyst.* 12. doi:10.1029/2010gc003478

McLean, N. M., Condon, D. J., Schoene, B., and Bowring, S. A. (2015). Evaluating Uncertainties in the Calibration of Isotopic Reference Materials and Multi-Element Isotopic Tracers (EARTHTIME Tracer Calibration Part II). *Geochim. Cosmochim. Acta* 164, 481–501. doi:10.1016/j.gca.2015.02.040

Meinert, L. D., Dipple, G. M., and Nicolescu, S. (2005). World Skarn Deposits: doi:10.5382/av100.11

Melfos, V., and Voudouris, P. (2017). Cenozoic metallogeny of Greece and potential for precious, critical and rare metals exploration. *Ore Geol. Rev.* 89, 1030–1057.

Mladenović, A., Trivić, B., and Cvetković, V. (2015). How Tectonics Controlled post-collisional Magmatism within the Dinarides: Inferences Based on Study of Tectono-Magmatic Events in the Kopaonik Mts. (Southern Serbia). *Tectonophysics* 646, 36–49. doi:10.1016/j.tecto.2015.02.001

Moritz, R., Noverraz, C., Márton, I., Marchev, P., Spikings, R., Fontignie, D., et al. (2014). Sedimentary-rock-hosted Epithermal Systems of the Tertiary Eastern Rhodopes, Bulgaria: New Constraints from the Stremtsi Gold prospect. *Geol. Soc. Lond. Spec. Publ.* 402, 207–230. doi:10.1144/sp402.7

Pamic, J., and Balen, D. (2001). Tertiary magmatism of the Dinarides and the adjoining South Pannonian Basin: an overview. *Acta Vulcan* 13, 9–24.

Paton, C., Woodhead, J. D., Hellstrom, J. C., Hergt, J. M., Greig, A., and Maas, R. (2010). Improved Laser Ablation U-Pb Zircon Geochronology through Robust Downhole Fractionation Correction. *Geochem. Geophys. Geosystems* 11. doi:10.1029/2009gc002618

Pecskay, Z., Eleftheriadis, G., Koroneos, A., Soldatos, T., and Christofides, G. (2003). K/Ar dating, geochemistry and evolution of the Tertiary volcanic rocks

(Thrace, northeastern Greece): Mineral exploration and sustainable development. Millpress: Rotterdam. 1229–1232.

Prelevic, D. (2005). Tertiary Ultrapotassic Volcanism in Serbia: Constraints on Petrogenesis and Mantle Source Characteristics. *J. Petrol.* 46, 1443–1487.

Prelevic, D., Foley, S. F., Cvetkovic, V., and Romer, R. L. (2004). Origin of Minette by Mixing of Lamproite and Dacite Magmas in Veliki Majdan, Serbia. *J. Petrol.* 45, 759–792. doi:10.1093/petrology/egg109

Reid, M. R., Vazquez, J. A., and Schmitt, A. K. (2011). Zircon-scale Insights into the History of a Supervolcano, Bishop Tuff, Long Valley, California, with Implications for the Ti-In-Zircon Geothermometer. *Contrib. Mineral. Petrol.* 161, 293–311. doi:10.1007/s00410-010-0532-0

Rezeau, Y., Moritz, R., Wotzlaw, J.-F., Tayan, R., Melkonyan, R., Ulianov, A., et al. (2016). Temporal and genetic link between incremental pluton assembly and pulsed porphyry Cu-Mo formation in accretionary orogens. *Geology* 44, 627–630.

Richards, J. P., and Kerrich, R. (2007). Special Paper: Adakite-Like Rocks: Their Diverse Origins and Questionable Role in Metallogenesis. *Econom. Geol.* 102, 537–576.

Richards, J. P. (2011). Magmatic to Hydrothermal Metal Fluxes in Convergent and Collided Margins. *Ore Geol. Rev.* 40, 1–26. doi:10.1016/j.oregeorev.2011.05.006

Richards, J. P. (2015). Tectonic, Magmatic, and Metallogenic Evolution of the Tethyan Orogen: From Subduction to Collision. *Ore Geol. Rev.* 70, 323–345. doi:10.1016/j.oregeorev.2014.11.009

Rickwood, P. C. (1989). Boundary Lines within Petrologic Diagrams Which Use Oxides of Major and Minor Elements. *Lithos* 22, 247–263. doi:10.1016/0024-4937(89)90028-5

Rohrlach, B. D., and Loucks, R. R. (2005). "Multi-million-year Cyclic Ramp-Up of Volatiles in a Lower Crustal Magma Reservoir Trapped below the Tampakan Copper-Gold deposit by Mio-Pliocene Crustal Compression in the Southern Philippines: Super Porphyry Copper and Gold Deposits," in *A Global Perspective: Adelaide*. PGC Publishing, 369–407.

Rohrlach, B. D., and Loucks, R. R. (2005). Multi-million-year cyclic ramp-up of volatiles in a lower crustal magma reservoir trapped below the Tampakan copper-gold deposit by Mio-Pliocene crustal compression in the southern Philippines: Super porphyry copper and gold deposits: A global perspective. Adelaide: PGC Publishing 2, 369–407.

Rohrmeier, M. K., von Quadt, A., Driesner, T., Heinrich, C. A., Handler, R., Ovtcharova, M., et al. (2013). Post-orogenic Extension and Hydrothermal Ore Formation: High-Precision Geochronology of the Central Rhodopian Metamorphic Core Complex (Bulgaria-Greece). *Econ. Geol.* 108, 691–718. doi:10.2113/econgeo.108.4.691

Rottier, B., Kouzmanov, K., Ovtcharova, M., Ulianov, A., Wälle, M., Selby, D., et al. (2020). Multiple rejuvenation episodes of a silicic magma reservoir at the origin of the large diatreme-dome complex and porphyry-type mineralization events at Cerro de Pasco (Peru). *Lithos* 376-377, 105766. doi:10.1016/j.lithos.2020.105766

Sasso, A. (1998). The Farallón Negro Group, Northwest Argentina: Magmatic, Hydrothermal and Tectonic Evolution and Implications for Cu-Au Metallogeny in the Andean Back-arc. *Soc. Econ. Geol. Newsletter* 34, 8–18.

Samperton, K. M., Schoene, B., Cottle, J. M., Brenhin Keller, C., Crowley, J. L., and Schmitz, M. D. (2015). Magma Emplacement, Differentiation and Cooling in the Middle Crust: Integrated Zircon Geochronological-Geochemical Constraints from the Bergell Intrusion, Central Alps. *Chem. Geol.* 417, 322–340. doi:10.1016/j.chemgeo.2015.10.024

Schefer, S., Cvetković, V., Fügenschuh, B., Kounov, A., Ovtcharova, M., Schaltegger, U., et al. (2011). Cenozoic Granitoids in the Dinarides of Southern Serbia: Age of Intrusion, Isotope Geochemistry, Exhumation History and Significance for the Geodynamic Evolution of the Balkan Peninsula. *Int. J. Earth Sci. (Geol Rundsch)* 100, 1181–1206. doi:10.1007/s00531-010-0599-x

Schmid, S. M., Fügenschuh, B., Kounov, A., Maţenco, L., Nievergelt, P., Oberhänsli, R., et al. (2020). Tectonic Units of the Alpine Collision Zone between Eastern Alps and Western Turkey. *Gondwana Res.* 78, 308–374. doi:10.1016/j.gr.2019.07.005

Schoene, B., Schaltegger, U., Brack, P., Latkoczy, C., Stracke, A., and Günther, D. (2012). Rates of Magma Differentiation and Emplacement in a Ballooning Pluton Recorded by U-Pb TIMS-TEA, Adamello Batholith, Italy. *Earth Planet. Sci. Lett.* 355-356, 162–173. doi:10.1016/j.epsl.2012.08.019

Schoene, B., Condon, D. J., Morgan, L., and McLean, N. (2013). Precision and Accuracy in Geochronology. *Elements* 9, 19–24. doi:10.2113/gselements.9.1.19

Seghedi, I., Downes, H., Vaselli, O., Szakács, A., Balogh, K., and Pécskay, Z. (2004). Post-collisional Tertiary-Quaternary Mafic Alkalic Magmatism in the Carpathian-Pannonian Region: a Review. *Tectonophysics* 393, 43–62. doi:10.1016/j.tecto.2004.07.051

Serafimovski, T., Stefanova, V., and Volkov, A. V. (2010). Dwarf copper-gold porphyry deposits of the Buchim-Damjan-Borov Dol ore district, Republic of Macedonia (FYROM). *Geol. Ore Deposits* 52, 179–195.

Serafimovski, T., and Boev, B. (1996). Metallogeny of the Kratovo–Zletovo volcano-intrusive complex. *Terranes Serbia* 356, 347–352.

Singer, B., and Marchev, P. (2000). Temporal evolution of arc magmatism and hydrothermal activity, including epithermal gold veins, Borovitsa caldera, southern Bulgaria. *Econom. Geol.* 95, 1155–1164.

Siron, C. R., Rhys, D., Thompson, J. F. H., Baker, T., Veligrakis, T., and Camacho, A. (2018). Structural Controls on Porphyry Au-Cu and Au-Rich Polymetallic Carbonate-Hosted Replacement Deposits of the Kassandra Mining District, Northern Greece. *Econom. Geol.* 113, 309–345.

Strmić Palinkaš, S., A Palinkaš, L., Mandić, M., Roller-Lutz, Z., and Pecskay, Z. (2016). 1039 Origin and K-Ar age of the phreatomagmatic breccia at the Trepča Pb-Zn-Ag skarn deposit, Kosovo: Implications for ore-forming processes. *Geologia Croatica* 69, 121–142.

Stojadinovic, U., Matenco, L., Andriessen, P. A. M., Toljić, M., and Foeken, J. P. T. (2013). The Balance between Orogenic Building and Subsequent Extension during the Tertiary Evolution of the NE Dinarides: Constraints from Low-Temperature Thermochronology. *Glob. Planet. Change* 103, 19–38. doi:10.1016/j.gloplacha.2012.08.004

Stojadinovic, U., Matenco, L., Andriessen, P., Toljić, M., Rundić, L., and Ducea, M. N. (2017). Structure and Provenance of Late Cretaceous-Miocene Sediments Located Near the NE Dinarides Margin: Inferences from Kinematics of Orogenic Building and Subsequent Extensional Collapse. *Tectonophysics* 710-711, 184–204. doi:10.1016/j.tecto.2016.12.021

Sun, S.-s., and McDonough, W. F. (1989). Chemical and Isotopic Systematics of Oceanic Basalts: Implications for Mantle Composition and Processes. *Geol. Soc. Lond. Spec. Publ.* 42, 313–345. doi:10.1144/gsl.sp.1989.042.01.19

Szymanowski, D., Wotzlaw, J.-F., Ellis, B. S., Bachmann, O., Guillong, M., and von Quadt, A. (2017). Protracted Near-Solidus Storage and Pre-eruptive Rejuvenation of Large Magma Reservoirs. *Nat. Geosci.* 10, 777–782. doi:10.1038/ngeo3020

Tapster, S., Condon, D. J., Naden, J., Noble, S. R., Petterson, M. G., Roberts, N. M. W., et al. (2016). Rapid thermal Rejuvenation of High-Crystallinity Magma Linked to Porphyry Copper deposit Formation; Evidence from the Koloula Porphyry Prospect, Solomon Islands. *Earth Planet. Sci. Lett.* 442, 206–217. doi:10.1016/j.epsl.2016.02.046

Taghipour, B., Moore, F., Mackizadeh, M. A., and Taghipour, S. (2013). Hydrothermal garnet in porphyry copper related skarn deposits, Ali-Abad, Yazd Province, Iran. *Iran. J. Sci. Technol.* A1, 11–22.

Toljić, M., Matenco, L., Ducea, M. N., Stojadinović, U., Milivojević, J., and Đerić, N. (2013). The Evolution of a Key Segment in the Europe–Adria Collision: The Fruška Gora of Northern Serbia. *Glob. Planet. Change* 103, 39–62. doi:10.1016/j.gloplacha.2012.10.009

Toljić, M., Matenco, L., Stojadinović, U., Willingshofer, E., and Ljubović-Obradović, D. (2018). Understanding Fossil Fore-Arc Basins: Inferences from the Cretaceous Adria-Europe Convergence in the NE Dinarides. *Glob. Planet. Change* 171, 167–184.

Urosević, M., Pavlović, Z., Klisić, M., Karamata, S., Malesevic, M., Stefanović, M., et al. (1973). *Basic Geological Map 1:100,000, Sheet Novi Pazar. Explanatory Note*. Belgrade: Federal Geological Institute, 1–77.

Ustaszewski, K., Kounov, A., Schmid, S. M., Schaltegger, U., Krenn, E., Frank, W., et al. (2010). Evolution of the Adria-Europe Plate Boundary in the Northern Dinarides: From Continent-Continent Collision to Back-Arc Extension. *Tectonics* 29. doi:10.1029/2010tc002668

von Quadt, A., Moritz, R., Peytcheva, I., and Heinrich, C. A. (2005). 3: Geochronology and Geodynamics of Late Cretaceous Magmatism and Cu-Au Mineralization in the Panagyurishte Region of the Apuseni-Banat-Timok-Srednogorie belt, Bulgaria. *Ore Geology. Rev.* 27, 95–126. doi:10.1016/j.oregeorev.2005.07.024

von Quadt, A., Erni, M., Martinek, K., Moll, M., Peytcheva, I., and Heinrich, C. A. (2011). Zircon Crystallization and the Lifetimes of Ore-Forming Magmatic-Hydrothermal Systems. *Geology* 39, 731–734. doi:10.1130/g31966.1

von Quadt, A., Gallhofer, D., Guillong, M., Peytcheva, I., Waelle, M., and Sakata, S. (2014). U-pb Dating of CA/non-CA Treated Zircons Obtained by LA-ICP-MS and CA-TIMS Techniques: Impact for Their Geological Interpretation. *J. Anal. Spectrom.* 29, 1618–1629. doi:10.1039/c4ja00102h

Voudouris, P., Mavrogonatos, C., Spry, P. G., Baker, T., Melfos, V., Klemd, R., et al. (2019). Porphyry and epithermal deposits in Greece: An overview, new discoveries, and mineralogical constraints on their genesis: Ore Geology Reviews, v. 107, p. 654–691. *Ore Geol. Rev.* 107, 654–691.

Winchester, J. A., and Floyd, P. A. (1976). Geochemical Magma Type Discrimination: Application to Altered and Metamorphosed Basic Igneous Rocks. *Earth Planet. Sci. Lett.* 28, 459–469. doi:10.1016/0012-821x(76)90207-7

Weis, P., Driesner, T., and Heinrich, C. A. (2012). Porphyry-Copper Ore Shells Form at Stable Pressure-Temperature Fronts Within Dynamic Fluid Plumes. *Science* 338, 1613–1616.

Wotzlaw, J.-F., Schaltegger, U., Frick, D. A., Dungan, M. A., Gerdes, A., and Günther, D. (2013). Tracking the Evolution of Large-Volume Silicic Magma Reservoirs from Assembly to Supereruption. *Geology* 41, 867–870. doi:10.1130/g34366.1

Conflict of Interest: TB was employed by the company Eldorado Gold Corporation.

The remaining authors declare that the research was conducted in the absence of any commercial or financial relationships that could be construed as a potential conflict of interest.